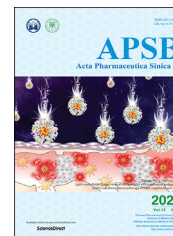




Chinese Pharmaceutical Association  
Institute of Materia Medica, Chinese Academy of Medical Sciences

Acta Pharmaceutica Sinica B

[www.elsevier.com/locate/apsb](http://www.elsevier.com/locate/apsb)  
[www.sciencedirect.com](http://www.sciencedirect.com)



ORIGINAL ARTICLE

# Allosteric inhibition reveals SHP2-mediated tumor immunosuppression in colon cancer by single-cell transcriptomics



Jian Gao<sup>a,†</sup>, Zhigui Wu<sup>a,†</sup>, Mingxia Zhao<sup>a,b,†</sup>, Rui Zhang<sup>c</sup>, Manru Li<sup>a</sup>, Dongdong Sun<sup>d</sup>, Haibo Cheng<sup>d</sup>, Xianjia Qi<sup>e</sup>, Yuxian Shen<sup>b</sup>, Qiang Xu<sup>a,f,\*</sup>, Hongqi Chen<sup>g,\*</sup>, Dijun Chen<sup>a,\*</sup>, Yang Sun<sup>a,f,\*</sup>

<sup>a</sup>State Key Laboratory of Pharmaceutical Biotechnology, Chemistry and Biomedicine Innovation Center (ChemBIC), School of Life Sciences, Nanjing University, Nanjing 210023, China

<sup>b</sup>Biopharmaceutical Research Institute, School of Basic Medical Sciences, Anhui Medical University, Hefei 230032, China

<sup>c</sup>Department of Colorectal Surgery, Cancer Hospital of China Medical University, Liaoning Cancer Hospital & Institute, Shenyang 110042, China

<sup>d</sup>The First Clinical College of Nanjing University of Chinese Medicine, Nanjing 210023, China

<sup>e</sup>Shanghai XuRan Biotechnology Co., Ltd., Shanghai 201109, China

<sup>f</sup>Jiangsu Key Laboratory of New Drug Research and Clinical Pharmacy, Xuzhou Medical University, Xuzhou 221004, China

<sup>g</sup>Department of General Surgery, Shanghai Jiao Tong University Affiliated Sixth People's Hospital, Shanghai 200233, China

Received 13 May 2021; received in revised form 27 July 2021; accepted 30 July 2021

## KEY WORDS

Tumor microenvironment;  
PTPN11;

**Abstract** Colorectal cancer (CRC), a malignant tumor worldwide consists of microsatellite instability (MSI) and stable (MSS) phenotypes. Although SHP2 is a hopeful target for cancer therapy, its relationship with innate immunosuppression remains elusive. To address that, single-cell RNA sequencing was

*Abbreviations:* APC, antigen-presenting cell; BTLA, B- and T-lymphocyte attenuator; CNVs, copy number variations; CRC, colorectal cancer; DSBs, double-strand breaks; GSEA, gene set enrichment analysis; KRAS, Kirsten rat sarcoma viral oncogene homolog; MAPK, mitogen-activated kinase; MSI, microsatellite instability; MSS, microsatellite stable; PCA, principal component analysis; PD-1, programmed cell death 1; scRNA-seq, single-cell RNA-sequencing; STING, stimulator of interferon genes; TME, tumor microenvironment; t-SNE, t-distributed stochastic neighbor embedding.

\*Corresponding authors.

E-mail addresses: [qiangxu@nju.edu.cn](mailto:qiangxu@nju.edu.cn) (Qiang Xu), [hqchen08@163.com](mailto:hqchen08@163.com) (Hongqi Chen), [dijunchen@nju.edu.cn](mailto:dijunchen@nju.edu.cn) (Dijun Chen), [yangsun@nju.edu.cn](mailto:yangsun@nju.edu.cn) (Yang Sun).

<sup>†</sup>These authors made equal contributions to this work.

Peer review under responsibility of Chinese Pharmaceutical Association and Institute of Materia Medica, Chinese Academy of Medical Sciences.

<https://doi.org/10.1016/j.apsb.2021.08.006>

2211-3835 © 2022 Chinese Pharmaceutical Association and Institute of Materia Medica, Chinese Academy of Medical Sciences. Production and hosting by Elsevier B.V. This is an open access article under the CC BY-NC-ND license (<http://creativecommons.org/licenses/by-nc-nd/4.0/>).

SHP099;  
STING;  
Type I interferon;  
Colorectal cancer;  
scRNA-seq;  
Macrophage

performed to explore the role of SHP2 in all cell types of tumor microenvironment (TME) from murine MC38 xenografts. Intratumoral cells were found to be functionally heterogeneous and responded significantly to SHP099, a SHP2 allosteric inhibitor. The malignant evolution of tumor cells was remarkably arrested by SHP099. Mechanistically, STING–TBK1–IRF3-mediated type I interferon signaling was highly activated by SHP099 in infiltrated myeloid cells. Notably, CRC patients with MSS phenotype exhibited greater macrophage infiltration and more potent SHP2 phosphorylation in CD68<sup>+</sup> macrophages than MSI-high phenotypes, suggesting the potential role of macrophagic SHP2 in TME. Collectively, our data reveals a mechanism of innate immunosuppression mediated by SHP2, suggesting that SHP2 is a promising target for colon cancer immunotherapy.

© 2022 Chinese Pharmaceutical Association and Institute of Materia Medica, Chinese Academy of Medical Sciences. Production and hosting by Elsevier B.V. This is an open access article under the CC BY-NC-ND license (<http://creativecommons.org/licenses/by-nc-nd/4.0/>).

## 1. Introduction

Colorectal cancer (CRC), a malignant epithelial tumor, which almost in all cases features as an adenocarcinoma, is the third most common cancer and the fourth leading cause of cancer-mortality worldwide<sup>1</sup>. Therefore, there is an urgent clinical demand for novel predictive marker and effective treatment. Carcinogenesis of CRC is directly associated with activating mutations of oncogenes such as the mitogen-activated kinase (MAPK) pathway gene, Kirsten rat sarcoma viral oncogene homolog (KRAS), which is the most prevalent predictive and prognostic oncogene with approximately 30%–50% detected in CRCs<sup>2</sup>. Obviously, the development and application of RAS/MAPK pathway inhibitors is a very crucial strategy for CRC treatments.

Recently, many studies have found that the prognosis of CRC is depending on the characteristics of immune landscape. Meanwhile, the degree of immune cell infiltration is closely related to the microsatellite status, which relies on the impairment of DNA mismatch repair (MMR) activity. Microsatellite instability (MSI) phenotype (15% in CRCs) is featured as deficiency of MMR activity and failure to repair double-strand breaks (DSBs). MSI phenotype, especially MSI-high (MSI-H) phenotype is identified as much more infiltrated immune cells and higher neoantigens expression for activating immune response than microsatellite stable (MSS) phenotype (85% in CRCs)<sup>3</sup>. Although MSI patients benefit from immune checkpoint inhibitors, some patients still fail to respond either initially or due to gradually developed resistance<sup>4</sup>. However, the mechanisms are poorly understood.

Endoplasmic reticulum membrane localized adaptor stimulator of interferon genes (STING) is a key intracellular pattern recognition receptor for cytosolic DNA signaling, which activates TBK1–IRF3 cascade to induce type I interferon production<sup>5</sup>. In tumor microenvironments, accumulated tumor-derived DNA and cGAMP can trigger the activation of antigen-presenting cells (APCs) for bridging innate and adaptive antitumor immune response<sup>6,7</sup>. Thus, much more studies tried to explore the value of STING as a potential target for cancer immunotherapy<sup>8–10</sup>. So, whether immunosuppression in the TMEs and sensitivity to immunotherapy of colon cancer is associated with destruction of DNA sensing cascades remains to further explore.

Tyrosine phosphatase SHP2 (encoded by *Ptpn11*) is a widely-expressed cytoplasmic phosphotyrosine phosphatase<sup>11,12</sup>. It

contains two SH2 domains (N-SH2 and C-SH2) followed by a tyrosine phosphatase (PTP) domain and a C-terminal tail with two phosphorylation sites. The crystal structure of SHP2 shows an auto-inhibited activity by its PTP and N-SH2 domain interaction which is an allosteric transition required to overcome after phosphotyrosine peptide stimulation<sup>13,14</sup>. SHP2 has been reported to be related to pathologic development of several disorders, such as hematological cancers<sup>15</sup>, solid tumors<sup>16</sup>, diabetes<sup>17,18</sup> and Noonan syndrome<sup>19</sup>. Activated SHP2 contributes to cell survival and proliferation by maintaining RAS-ERK signaling pathway activation<sup>20</sup>. Furthermore, SHP2 is a major downstream molecule required for B- and T-lymphocyte attenuator (BTLA) and programmed cell death 1 (PD-1) immune checkpoint pathways. Hence, intervention of SHP2 is a potential approach for cancer therapy<sup>21–23</sup>. Notably, allosteric inhibitors have inspired a novel strategy to selectively target SHP2 by binding to the nonanalytic sites, especially for anti-tumor therapy<sup>24–28</sup>. To date, four allosteric inhibitors such as JAB-3068, TNO155, RMC-4630, RLY-1971 have already entered clinical trials for the solid tumors treatment<sup>29</sup>.

The previous work of our group about SHP2 in T cell indicated that SHP2 depletion in T cells triggered an anti-tumor immunity against colitis-associated cancer in mice<sup>30</sup>. SHP2 inhibition enhanced cytotoxic T-cell related antitumor immune response and synergized with PD-1 blockade<sup>31</sup>. However, the role of SHP2 in other cell types of TMEs is still unclear. Therefore, we performed single-cell RNA sequencing to explore the contribution of SHP2 inhibition to immunotherapy and tumor response. Our result found that intratumoral cells was functionally heterogeneous of different responses to SHP099, a SHP2 allosteric inhibitor with nanomolar affinity<sup>24</sup>. Using pseudotime analyses, we revealed that SHP099 treatment could intervene the tumor malignant evolution. Mechanistically, SHP099 enhanced type I interferon signaling both in cancer cells and infiltrating immune cells, especially in T cell and macrophages by regulating STING–TBK1–IRF3 pathway. Moreover, colon tissue samples from the MSS phenotypes of CRC patients exhibited greater CD68<sup>+</sup> macrophages infiltration, more potent phosphorylation of SHP2 in CD68<sup>+</sup> macrophages, and lower IFN- $\beta$  expression compared to that of MSI-H phenotypes, suggesting the potential role of macrophagic SHP2 in TME. These data reveal SHP2 allosteric inhibition remodels anti-tumor microenvironment, indicating that SHP2 is a promising target for colon cancer immunotherapy.

## 2. Materials and methods

### 2.1. Mice

Myeloid-specific SHP2 knockout mice (*Ptpn11<sup>Lyz2-/-</sup>*) were generated by crossing *Ptpn11<sup>fllox/flox</sup>* mice with *Lyz2-Cre* transgenic mice. C57BL/6 mice (6–8 weeks old, 20–22 g) were purchased from the GemPharmatech Co., Ltd. (Nanjing, China). Mice were housed under specific-pathogen-free (SPF) conditions ( $22 \pm 2$  °C,  $55 \pm 10\%$  humidity and 12 h light–dark cycle), and supplied with sterilized food and water. Animal welfare and experimental procedures were carried out strictly in accordance with the Guide for the Care and Use of Laboratory Animals (National Institutes of Health, USA) and the related ethical regulations of Jiangsu Province and our university. All efforts were made to minimize animals' suffering and to reduce the number of animals used.

### 2.2. Reagents

SHP099 (Cat. #HY-100388) and SHP099 hydrochloride (Cat. #HY-100388A) were purchased from MedChemExpress (Monmouth Junction, NJ, USA). 2',3'-cGAMP (Cat. #tlrl-nacga23) was purchased from InvivoGen (San Diego, CA, USA). ELISA Kits for human and mouse IFN- $\beta$  were purchased from Multi Sciences Biotech Co., Ltd. (Hangzhou, China). Anti-p-TBK1 (Cat. #5483) and anti-p-IRF3 (Cat. #4947) were purchased from Cell Signaling Technology (Beverly, MA, USA). Anti-TBK1 (Cat. #DF7026) was purchased from Affinity Biosciences (Cincinnati, OH, USA). Anti-IRF3 (Cat. #11312-1-AP) and anti-STING (Cat. #19851-1-AP) were purchased from Proteintech Group (Rosemont, IL, USA). Anti-SHP2 (Cat. #sc-7384) was purchased from Santa Cruz Biotechnology (Santa Cruz, CA, USA). Anti- $\beta$ -actin (Cat. #M20011) was purchased from Abmart (Shanghai, China). Alexa Fluor 488 goat anti-rabbit IgG (H + L) cross-adsorbed secondary antibody (Cat. #A11008) was purchased from ThermoFisher Scientific (Waltham, MA, USA). All other chemicals were obtained from Sigma–Aldrich (St. Louis, MO, USA).

### 2.3. Cell culture

MC38 cell line was obtained from Cell Resource Center of the Institutes of Biomedical Sciences at Fudan University (Shanghai, China) and maintained in the appropriate culture medium suggested by suppliers. THP1 cell line was obtained from Shanghai Institute of Cell Biology (Shanghai, China) and cultured with RPMI 1640 (Gibco, Grand Island, NY, USA) containing 10% FBS in 5% CO<sub>2</sub> at 37 °C.

Bone marrow cells were flushed out from the femurs and tibias of female C57BL/6 mice. After centrifugation for 5 min at 300 $\times$ g, erythrocytes were eliminated and the remaining cells were cultured with DMEM supplemented with 10% fetal bovine serum and 10 ng/mL M-CSF (PeproTech, Rock Hill, NJ, USA; Cat. #315–02). Culture fluid was exchanged with culture medium every 3 days. Under these conditions, adherent macrophages were obtained within 7 days. Cells were harvested and seeded on 12-well plates without M-CSF for 6 h, then the cells were used for the experiments as BMDMs.

### 2.4. Murine MC38 colon cancer xenograft model

C57BL/6 mice were inoculated with  $1 \times 10^6$  MC38 cells into the right flank. 5 days after the injection, the MC38 tumor-bearing

mice (an average size of 100 mm<sup>3</sup>) were distributed into 2 groups ( $n = 5$  in each group) and treated with PBS, SHP099 hydrochloride (5 mg/kg, i. g., every day) for an additional 14 days. Tumor tissues were excised on Day 19.

WT and *Ptpn11<sup>Lyz2-/-</sup>* mice were subcutaneously injected with  $1 \times 10^6$  MC38 colon cancer cells. Five days after the injection, tumor volumes were measured every 2 days and calculated using Eq. (1):

$$\text{Tumor volume} = 0.5 \times L_1 \times (L_2)^2 \quad (1)$$

where  $L_1$  and  $L_2$  are the long and short diameters of the tumor mass, respectively. Tumor tissues were excised on Day 23.

### 2.5. cDNA library construction and single-cell RNA-seq

Solid tumors from mice were excised and mechanically dissociated into single cells using Tumor Dissociation Kit (Miltenyi Biotec, Cat. #130-096-730). Single cells were captured in the 10  $\times$  Genomics Chromium Single Cell 3' Solution, and RNA-seq libraries were prepared following the manufacturer's protocol (10  $\times$  Genomics). The libraries were subjected to high-throughput sequencing on an Illumina HiSeq X Ten PE150 platform, and 150-bp paired-end reads were generated.

### 2.6. Process and quality control of the single-cell RNA-seq data

Single-cell RNA-seq data for each experiment were processed with *cellranger* count (10  $\times$  Genomics CellRanger [v3.1.0]) based on the mouse reference genome GRCm38 (mm10). Digital gene expression matrices were analyzed in R (v3.6.0), using the Seurat (v3.2.0) package<sup>32</sup>. Cells were filtered by the number of UMIs (less than 6500 UMIs) and percentage of mitochondrial genes ("percent.mt" lower than 10%), yielding a total of 7934 and 7881 cells for the SHP099 and PBS experiments, respectively. Normalization was performed with the *SCTransform*<sup>33</sup> function with regression of percentage of mitochondrial genes. For integration, 3000 shared highly variable genes were identified using the *SelectIntegrationFeatures* function. Integration anchors were identified based on these genes using the *FindIntegrationAnchors*<sup>34</sup> function with a "SCT" normalization method. The data were then integrated using the *IntegrateData* function. Principal component analysis (PCA) and t-distributed stochastic neighbor embedding (t-SNE) dimension reduction with the top 30 principal components were performed. A nearest-neighbor graph using the 30 dimensions of the PCA reduction was calculated using *FindNeighbors*, followed by clustering using *FindClusters* with a resolution of 0.8. Candidate marker genes for each cell cluster were identified by the *FindAllMarkers* function. For each cluster of cells, group-specific differentially expressed genes were identified using the Wilcoxon Rank Sum test as implemented in *FindAllMarkers*.

### 2.7. Annotating cell clusters

For each cell cluster identified as above, a cell type was assigned to it by using a combination of differentially expressed genes and known gene signatures (Supporting Information Table S1). Enrichment GO categories (Fig. 1F) for significantly expressed markers (FDR < 0.001) in each cell cluster were identified by *enrichGO* in the R package clusterProfiler (3.11.1). In order to

identify specific biological pathways enriched in each cell cluster, gene set enrichment analysis (GSEA) was performed based on the log-transformed fold change of gene expression, as implemented in the *gseGO* and *gseKEGG* function.

Chromosomal copy number variations (CNVs) were inferred from the single cell gene-expression data using the inferCNV

(1.3.3) R package. On a sample-by-sample basis, the immune and fibroblast cells (non-malignant cells) were used as a reference to estimate CNVs in the cancer-related cells. To run inferCNV, a gene location file, which contains the chromosomal start and end positions for each gene, were created by BioMart (v3.11)<sup>35,36</sup>, and a cutoff the minimum average read counts per gene among

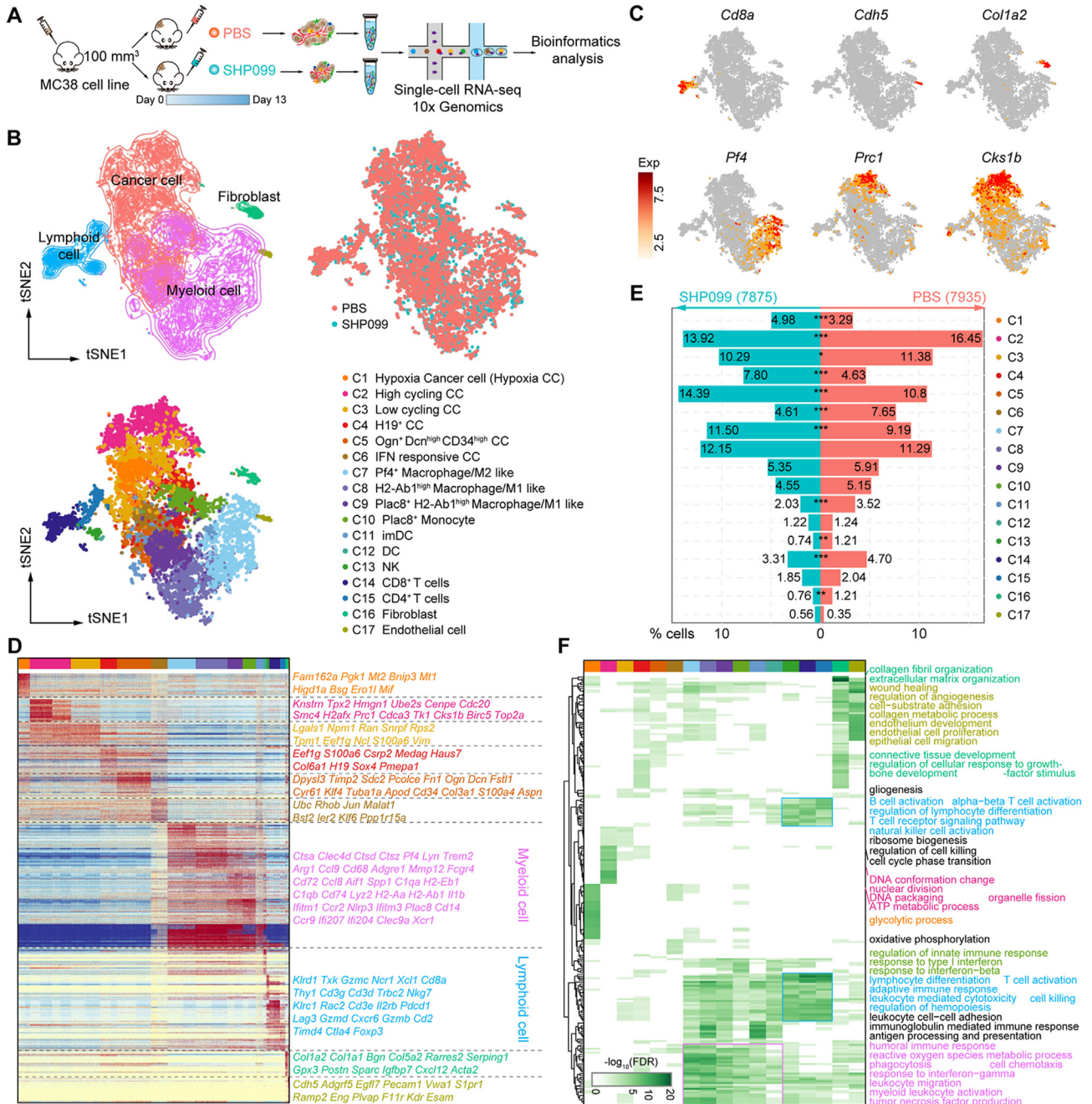


**Figure 1** Cell type identification and characterization in murine MC38 colon cancer xenograft model. (A) Overview of the scRNA-seq experiment. (B) t-stochastic neighbor embedding (t-SNE) plot of all cells colored by their cell type/identity (top left and bottom left) or by their sample origin (top right). The color code is consistent through all figures. (C) Expression of example marker genes. (D) Heatmap showing differentially expressed genes (DEGs) across cell clusters. Example marker genes are highlighted. Red: high expression; blue: low expression. (E) Bar plots showing the percentage (%) of cell types in the experimental groups of PBS and SHP099. Significant differences between the two groups were calculated by Fisher’s exact test followed by Benjamini-Hochberg correction. \**P* < 0.05; \*\**P* < 0.01 and \*\*\**P* < 0.001. (F) Enriched biological pathways for DEGs in each cell clusters.

reference cells was set to 0.1. Putative CNV regions were identified by a hidden Markov model (HMM), and the output was further denoised a Bayesian latent mixture model. In this regard, the threshold of BayesMaxPNormal parameter was set to 0.5 to filter out low-probability CNVs.

### 2.8. Pseudo-time lineage trajectory

Monocle 2 (<http://cole-trapnell-lab.github.io/monocle-release>) was used to infer the pseudotime trajectories of tumor cells to identify and to visualize pseudotime-dependent gene expression. Monocle orders cells by learning an explicit principal graph from the single cell genomics data with Reversed Graph Embedding, which robustly and accurately resolves complicated biological processes. All pseudotime-dependent genes were visualized by the `plot_pseudotime_heatmap` function taking a `CellDataSet` object. Lineage trajectory plot and smooth expression curves based on `CellDataSet` were generated by `plot_cell_trajectory` and `plot_genes_in_pseudotime` respectively<sup>37,38</sup>.

### 2.9. Quantitative real-time PCR analysis

Total RNA was extracted from cells using RNAiso Plus reagent (Takara, Cat. #9109) and reverse transcribed to cDNA and subjected to quantitative PCR, which was performed with the BioRad CFX96 Touch™ Real-Time PCR Detection System (BioRad, CA, USA) and ChamQ Universal SYBR qPCR Master Mix (Vazyme, Cat. #Q711-02-AA), and threshold cycle numbers were obtained using BioRad CFX manager software version 5.0. The program for amplification was 1 cycle of 95 °C for 2 min followed by 40 cycles of 95 °C for 15 s and 60 °C for 30 s. The primer sequences used in this study were listed in [Supporting Information Table S2](#).

### 2.10. Western blot analysis

Western blot analysis was performed as previously described<sup>39</sup>.

### 2.11. Immunofluorescence

The treated cells were fixed and blocked in blocking buffer (1 × PBS, 5% BSA, 0.01% Triton X-100) for 1 h. After incubated with primary antibodies (1:200) at 4 °C overnight, cells were washed with PBS 5 times, stained with fluorophore-conjugated secondary antibodies (1:500) at room temperature for 90 min and counter-stained with DAPI for 2 min. After washed 5 times, the cells were observed with a confocal laser scanning microscope (LSM880, Zeiss, Oberkochen, Germany).

For tumor tissue sections, the sections were rehydrated, washed and blocked in blocking buffer (1 × PBS, 5% anti-goat serum, 0.01% Triton X-100) for 1 h, and then incubated with primary antibodies (1:200) at 4 °C overnight. Sections were then washed with PBS 5 times and stained with fluorophore-conjugated secondary antibodies (1:500) at room temperature for 90 min. After washed 5 times, samples were observed with a scanning microscope (Slideview VS200, Olympus, Lake Success, NY, USA).

### 2.12. Flow cytometry

For multicolor flow cytometry analysis, solid tumors from mice were excised and mechanically dissociated using Tumor

Dissociation Kit, Mouse (Miltenyi Biotec) on Day 14. After blocked by species-matched anti-CD16/32 antibodies (BD Pharmingen) for 10 min on ice, single cell suspensions were stained with anti-mouse CD45-Alexa Fluor 700 (clone 30-F11, Cat. #560510), NK1.1-BB700 (clone PK136, Cat. #566502), CD3e-BV510 (clone 145-2C11, Cat. #563024), CD4-BV605 (clone RM4-5, Cat. #563151), CD8a-BB515 (clone 53-6.7, Cat. #564422), F4/80-APC (clone BM8, Cat. #123116), CD86-PE-Cy7 (clone GL-1, Cat. #105014), CD206-BV421 (clone C068C2, Cat. #141717), pSHP2-PE (pY542, clone L99-921, Cat. #560389) for 30 min. Gates were set by fluorescence minus one control for the cell markers other than pSHP2 which was set based off of isotype control. Then the samples were analyzed by Attune NxT (Thermo Fisher). The gating strategies used are including in [Supporting Information Fig. S1](#).

### 2.13. Single cell RNA-seq analysis of clinical colorectal cancer samples

Single cell RNA-seq files was obtained from GSE132465 in NCBI Gene Expression Omnibus (GEO) database. GSE132465 is a single-cell 3' RNA sequencing dataset on 63,689 cells from 23 CRC patients with 23 primary colorectal cancer and 10 matched normal mucosa samples<sup>40</sup>. Cell annotation was accessible both in GEO and its citation. Downstream analysis was performed by using Seurat and ggplot2 R package. Somatic copy number aberrations were inferred from the single cell gene-expression data using the CopyKAT (1.0.4) R package<sup>41</sup>. Goblet cells from normal mucosa samples were identified as normal (diploid) cells passed to parameter 'norm.cell.names'. Cells with less than five genes on each chromosome were filtered. The parameters 'low. DR' and 'up. DR' were set to default value 0.05 and 0.2 respectively. Eventually, cells with extensive genome-wide copy number aberrations (aneuploidy) were considered as malignant cells.

### 2.14. Human specimens

All human colorectal cancer samples were approved by the Ethics Institutional Review Board of the Affiliated Hospital of Nanjing University of Chinese Medicine (Nanjing, China; study number 2020NL-094-02). The patients' information in this study were listed in [Supporting Information Table S3](#).

### 2.15. Statistical analysis

Statistical analysis was performed using GraphPad Prism 8.0. One-way ANOVA with a Tukey's multiple comparisons post-test was used to compare the groups. Paired or unpaired Student's *t*-test was used to detect statistically significant treatment effects when only two groups were compared.  $P < 0.05$  were considered as statistically significant (\* $P < 0.05$ , \*\* $P < 0.01$ ), ns represents no significance. All data are expressed as mean ± SEM.

### 2.16. Data availability

Raw data for single cell RNA-seq samples are available in the Gene Expression Omnibus (GEO) database as accession number GSE164908.

### 3. Results

#### 3.1. Intratumoral cell types defined by scRNA-seq

We collected the single cells from murine MC38 xenograft tumors in PBS and SHP099 treatment groups (Supporting Information Fig. S2). The transcriptomes of individual cells were obtained by scRNA-seq using a droplet-based 10 × Genomics platform. After quality control and filtering, 7934 and 7881 transcriptomes of single cells for the SHP099 and PBS treatments were obtained (Fig. 1A and Supporting Information Fig. S3). Five major cell types including cancer cell, lymphoid cell, myeloid cell, fibroblast and endothelial cell were defined as the major population in TME (Fig. 1B). Unsupervised clustering with t-SNE revealed 17 sub cell clusters, which were annotated by known or putative markers (Fig. 1B and D). Cancer-related cells (C1-6) represented more than half (~55%) of all cells (Fig. 1E). These cell clusters were *Ptprc* negative (*Cd45*<sup>-</sup>) and functionally heterogeneous. For example, these subsets were generally enriched for genes such as hypoxia marker *Bnip3* and *Ero11*, proliferation marker *Cdc20* and *Top2a*<sup>42</sup>, epithelial–mesenchymal transition marker *Vim*, and extracellular matrix gene *Dcn* (*Decorin*) and *Col3a1* (Fig. 1D). Cell clusters C8-12 were classified as myeloid cell as they expressed myeloid markers, such as *Pf4*, *Arg1*, *Lyz2*, *Spp1*, *Plac8* and *Cd14*, while clusters C13–15 were annotated as lymphoid cell based on known markers such as *Klrd1*, *Cd3d*, *Cd8a*, *Cxcr6* and *Foxp3*<sup>43</sup>. The rest two clusters, fibroblast (C16) and endothelial cell (C17), count for less than 2% of all cells (Fig. 1E), which were identified by known markers *Colla1*, *Colla2* and *Acta2* (for fibroblast)<sup>44</sup>, and *Cdh5*, *Pecam1*, *Kdr* (for endothelial cell; Fig. 1D). Accordingly, highly expressed genes in distinct cell clusters were specially enriched for specific biological pathways in line with their cell type origin (Fig. 1F). For example, fibroblast (C16) was enriched for ‘extracellular matrix organization’ and endothelial cell (C17) was enriched for ‘wound healing’. Interestingly, although these cell clusters were proportionally distributed between the PBS and SHP099 groups, the composition of cancer- and immune-related cells singularly changed between the two treatment groups (Fig. 1E). Overall, our single cell transcriptome data revealed the cell clusters corresponded to almost major known cell types and provided an important resource to study the molecular mechanism underlying the role of SHP2 in TME.

#### 3.2. Characterization of tumor cells with functional heterogeneity and transcriptome dynamics upon SHP099 treatment

Among the annotated cell types, all the cancer-related cell subclusters showed significantly discrepant upon SHP099 treatment (Fig. 1E). To figure out molecular alterations of the SHP099 treatment, we isolated these cancer cells for further analysis (Fig. 2A). Among these, C1 was defined as hypoxia cancer cell according to the marker genes including *Bnip3*, *Higd1a*, *Ero11* and related pathways, such as ‘response to hypoxia’, ‘ATP metabolic process’, ‘oxidative phosphorylation’ and ‘intrinsic apoptotic signaling pathway’ (Supporting Information Table S4). C2 was characterized as high cycling cancer cell result from the marker genes *Knstrn*, *Tpx2*, *Cenpe*, *Cdc20*, *Birc5*, *Top2a* and enriched pathways ‘nuclear division’, ‘organelle fission’, ‘chromosome segregation’ and ‘cell cycle phase transition’ (Supporting Information Fig. S4A and Table S4). C5 was inclined to express

extracellular matrix. Notably, C4 and C6 were immunoreactive, enriched for the activation of innate immune ‘response to interferon-beta’ particularly. When comparing cancer cells from PBS and SHP099 groups, we found 21 differentially expressed genes (Fig. 2B and C). Interestingly, most of these differentially expressed genes were upregulated in SHP099-treated cancer cells, including JUN/FOS heterodimer complex (*Jund*, *June*, *Fos* and *Fosb*), extracellular matrix (*Aspn*, *Postn* and *Ogn*) and type I interferon inducible genes (*Ifit1* and *Ifit2712a*) (Fig. 2B and D). Accordingly, biological pathways such as ‘response to interferon/virus’ and ‘lymphocyte migration’ (immunologic) were highly active in the SHP099-treated cancer cells, while survival-related pathways were enriched in upregulated genes from the non-treatment group (Fig. 2E and F). Given the association between cancer and large-scale genomic alterations, we inferred copy-number variations (CNVs) from scRNA expression by comparing data between cancer cells and non-cancer cells (including immune and stromal cells; Fig. 2G). We further analyzed CNV-associated transcription factors (TFs) as their major impact on shaping cell transcriptome dynamics. We found 168 CNV-associated TFs in all the cancer-related cell subclusters (Fig. 2H). Compared to PBS-related cancer cells (non-treatment), cancer cells of the SHP099 group largely gained TF expression intensities across the genome (Fig. 2H), including proto-oncogene *Myc*, *Fosb* and *Fos*, were also enriched for ‘cell differentiation’ and ‘chromatin remodeling’ (Supporting Information Table S5). This finding is consistent with the above observation that cancer cells of the SHP099 group showed more number of upregulated genes (Fig. 2B).

#### 3.3. SHP099 restricts cancer malignant evolution

While the above analysis revealed heterogeneity among tumor cells, we also wondered whether SHP099 could intervene the tumor differentiation trajectories. When projecting all the cancer-related cells onto the pseudotime, we found that these cells were arranged into a major trajectory with three bifurcations and 7 states (Supporting Information Fig. S5A and S5B). Specifically, the *Ogn*<sup>+</sup> *Dcn*<sup>high</sup> *Cd34*<sup>high</sup> subcluster was identified as the principal progenitor and a conspicuous malignant evolution toward the cycling cancer subclusters (Fig. 3A). Moreover, the evolution was arrested and blocked before node 3 after SHP099 treatment (Fig. 3B). Furthermore, we analyzed gene expression dynamics, identified five major pseudotime-dependent gene clusters and determined many similar cell fates genes, such as *Top2a*, *Cdk1* and *Birc5* (Fig. 3C; Fig. S5C and S5D). These proliferation marker genes (such as *Top2a* and *Cdk1*) were distributed at the end of trajectory with increased density and expression levels (Fig. 3D), while *Ogn* showed an opposite trend (Fig. 3F). Notably, a differentiation tendency toward IFN response cancer cell state with SHP099 treatment was identified (Fig. 3A and B), and *Cxcl10* were distributed at the bifurcation 1 and showed increased expression in this group (Fig. 3E). Collectively, these results suggest SHP099 inhibits cancer malignant evolution.

#### 3.4. Enhanced interferon signaling by transcriptome signatures upon SHP099 treatment

Our previous work revealed that SHP099-mediated SHP2 inhibition elevated proportion and function of CD8<sup>+</sup> IFN- $\gamma$ <sup>+</sup> T cells to enhanced anti-tumor responses<sup>31</sup>. We analyzed the single-cell gene expression patterns of T cells. Three subset cell clusters

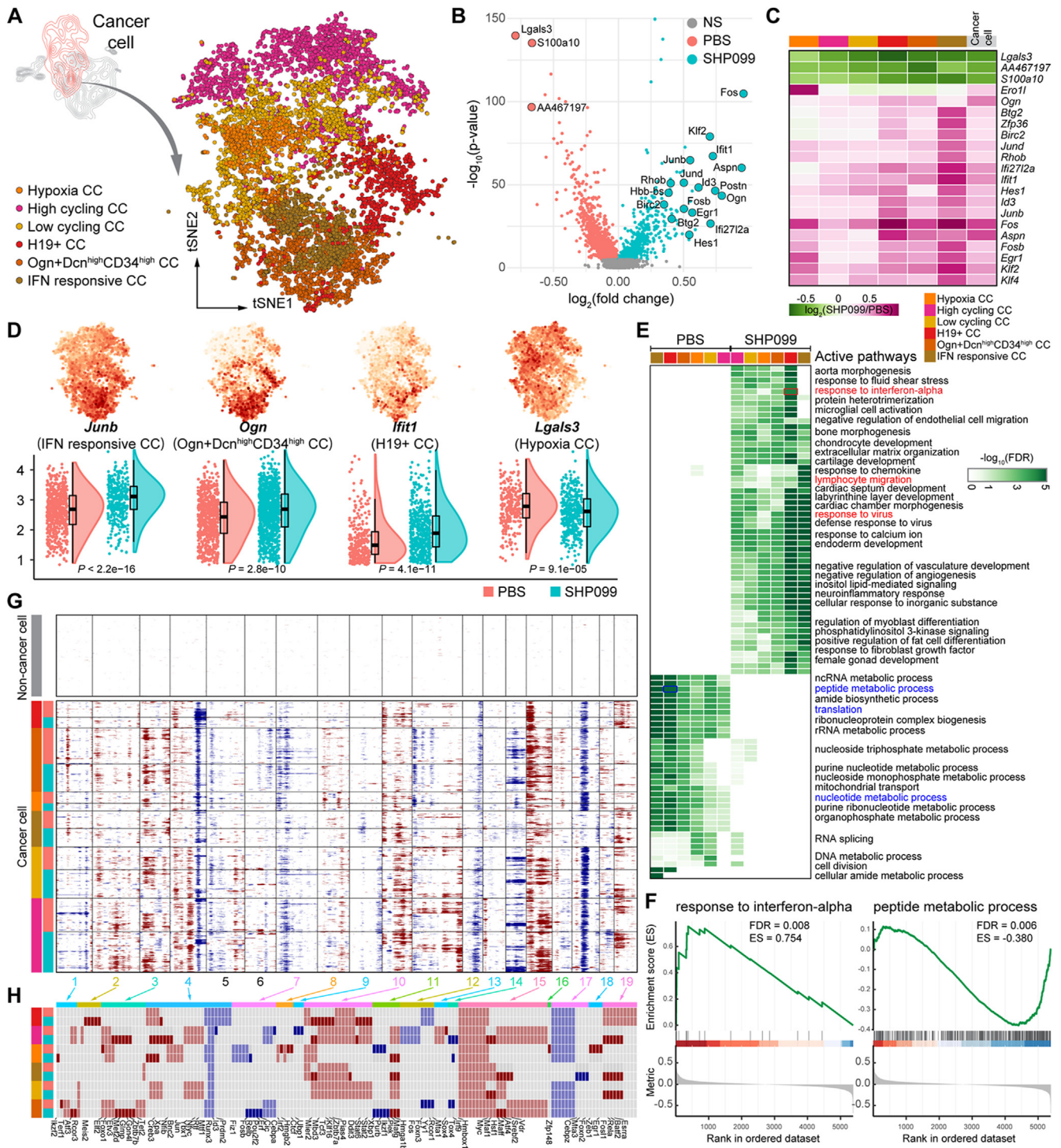


**Figure 2** Transcriptome signatures and dynamics upon SHP099 treatment in cancer cells. (A) t-SNE plot of cancer cell sub-clusters. (B) Volcano plot showing transcriptome dynamics between PBS and SHP099 in cancer cells. Significantly differentially expressed genes (DEGs; with adjusted  $P$ -value  $< 1.0 \times 10^{-5}$ ) are colored according to experimental groups. Top DEGs are highlighted. NS: not significant. (C) Expression difference of top DEGs between PBS and SHP099 in cancer cells and associated sub-clusters. (D) Examples of DEGs. t-SNE heatmaps show gene expression levels (top) and raincloud plots show expression difference between PBS and SHP099 in the dominant cell sub-clusters (bottom). (E) Gene set enrichment analysis (GSEA) of transcriptome dynamics upon SHP099 treatment in different cancer cell sub-clusters. Top active gene ontology (GO) biological pathways are shown in the heatmap. Examples of selected pathways (in red boxes) are shown in (F). (G) Landscape of inferred large-scale chromosomal copy number variations (CNVs) distinguishing cancer cells and non-cancer cells. Gained (red) or loss (blue) CNVs were inferred by averaging expression over 100-gene stretches on each chromosomes. Cancer cell sub-clusters are colored according to cell types or experimental groups. (H) Heatmap showing CNV-associated transcription factors (TFs). Difference in CNVs between PBS and SHP099 is colored in dark red (CNV gain) or dark blue (CNV loss).

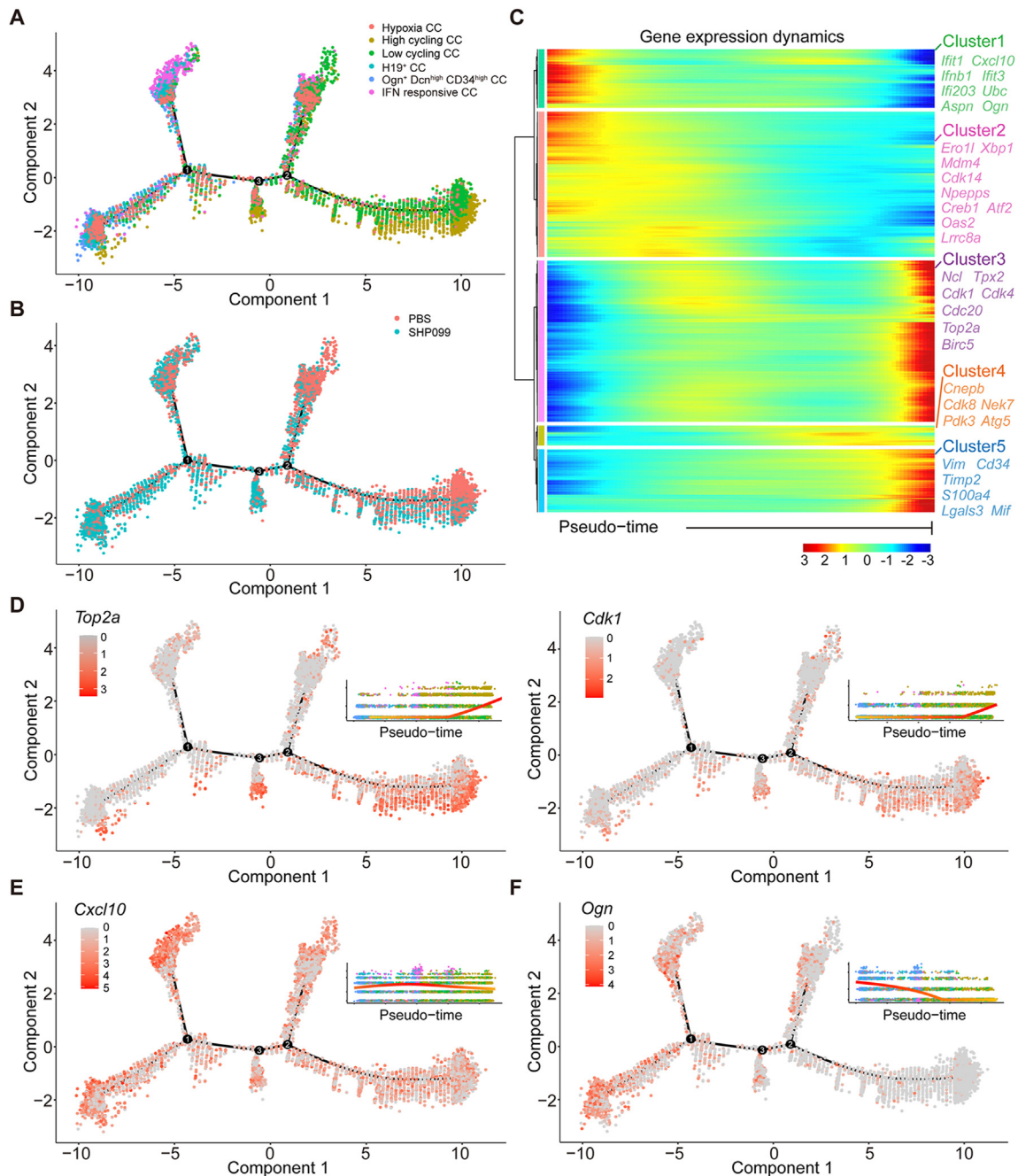


**Figure 3** Pseudotime analyses reveal cancer cell malignant differentiation trajectories interfered by SHP099 treatment. (A) Pseudotime ordering on cancer cells into a major trajectory with three bifurcations. (B) Distribution on the pseudotime trajectory of PBS and SHP099 groups. (C) Gene expression dynamics analysis was performed on pseudotime identified five gene clusters pseudotime-dependent genes. Heatmap of the expression levels for all differentially expressed genes and representative genes for each cluster are shown. (D) Feature plots of expression distribution for *Top2a*, *Cdk1*, *Cxcl10* and *Ogn* across pseudotime.

(CD8<sup>+</sup> T cell, CD4<sup>+</sup> T cell and NK) were identified (Fig. 4A) on the basis of their respective defined surface markers (*Cd3e*, *Cd4*, *Cd8a*, *Foxp3*, *Klrb1c* and *Klrd1*; Fig. 4B). As expected, “regulation of T cell activation” related pathways were highly activated in the whole T cell cluster compared with other cell clusters (Fig. 4C and D), although each subclusters of T cells enriched some specific biological pathways based on their corresponding highly expressed genes (Fig. S4B). Differential gene expression analysis between PBS and SHP099 groups revealed elevated expression of

T cell activation genes (*Cxcr6* and *Tnfrsf18*) and IFN-induced genes (*Bst2*, *Icos*, *Ifi1* and *Ifi203*) upon SHP099 treatment (Fig. 4E and G). In particular, the changes in expression profoundly occurred in a subcluster specific manner (Fig. 4F), which is in agreement with pathway enrichment analysis of highly expressed genes in each subclusters (Fig. 4H). For instance, comparison of cell subclusters between PBS and SHP099 groups revealed the overrepresentation of ‘response to type I interferon’ in CD8<sup>+</sup> T cells, while ‘interferon-gamma production’ and

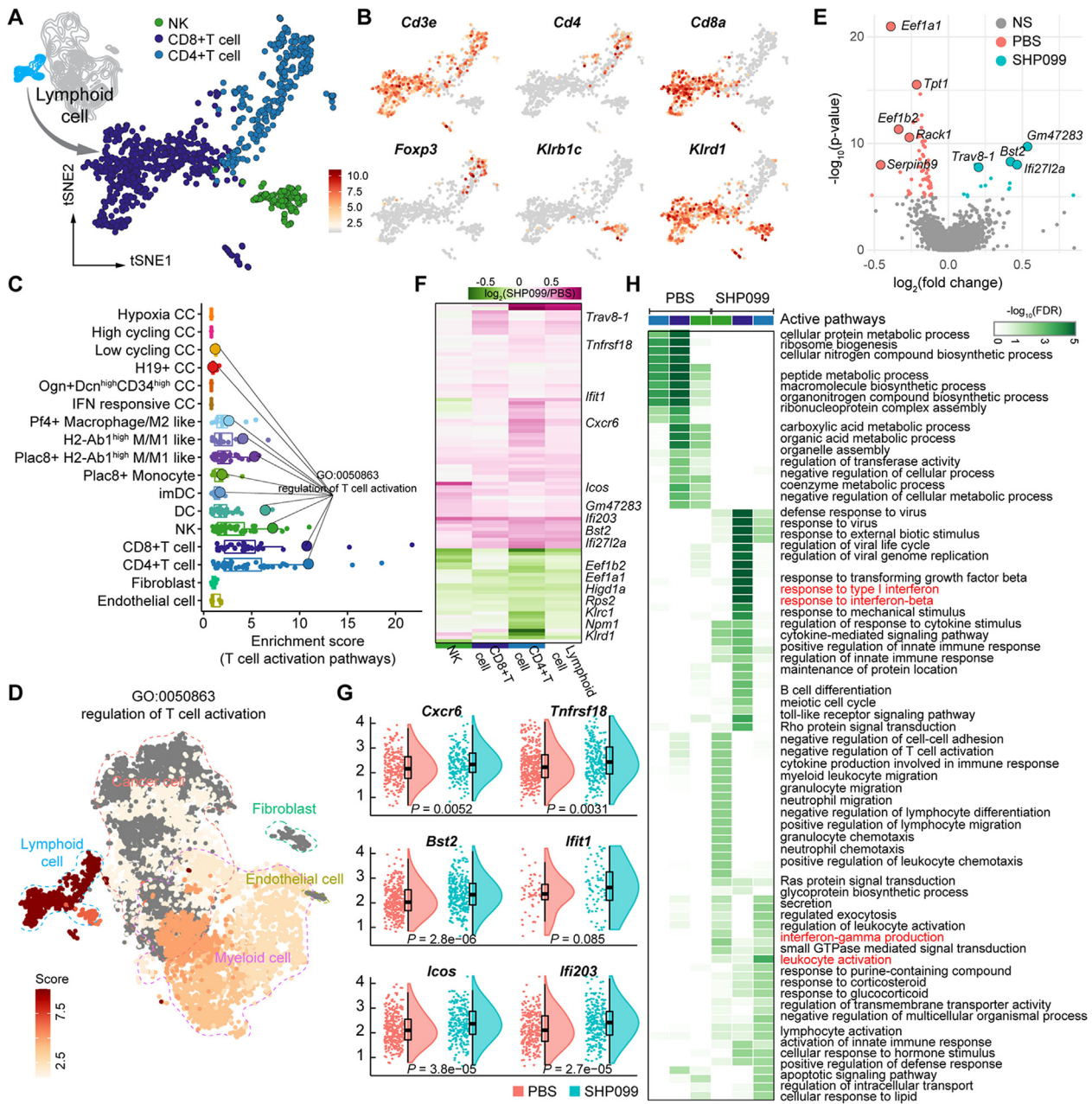


**Figure 4** Transcriptome dynamics of lymphoid cell. (A) t-SNE plot of lymphoid cell sub-clusters. (B) t-SNE plots of expression for selected marker genes. (C) Enrichment of “T cell activation” pathways in different cell clusters. The pathway of “regulation of T cell activation” (GO: 0050,863) is highlighted in large-size dots, and the corresponding enrichment score for this pathway is visualized in the t-SNE plot in (D). (E) Volcano plot showing all genes that were differentially expressed (with corrected  $P$ -value  $< 1.0 \times 10^{-5}$ ) between PBS and SHP099. Top differentially expressed genes (DEGs) are highlighted. NS: not significant. (F) Heatmap showing top DEGs between PBS and SHP099. The average fold-change (FC) of each gene (row) in SHP099 relative to PBS cells was plotted for each sub-clusters (column). Pink indicates higher expression in SHP099 cells and green indicates higher expression in PBS cells. (G) Raincloud plots show expression difference for lymphoid cells from PBS and SHP099 groups. (H) Gene set enrichment analysis (GSEA) applied on lymphoid cell expression data by comparing cells from PBS and SHP099 groups.

‘leukocyte activation’ in NK cells upon SHP099 treatment (Fig. 4H).

Following our scRNA-seq findings above, type I interferon signaling response was indicated enhanced in both cancer cells and lymphoid cells, but not in fibroblasts (Supporting Information Fig. S6). We asked to what extent this signaling response contributes to in myeloid cells. We applied a similar analysis on

myeloid cells (Fig. 5), of which six subclusters were identified based on known markers (*Cd14*, *Plac8*, *Cd68*, *H2-Ab1*, *Iil1b*, *Pf4*, *C1qc*, *Arg1*; Fig. 5A and B). All the myeloid subclusters displayed overrepresentation of “activation of immune response” based on highly expressed genes in each subclusters (Fig. 5C and D). To identify changes in expression associated with SHP099 treatment, we performed differentially expressed gene analysis in myeloid

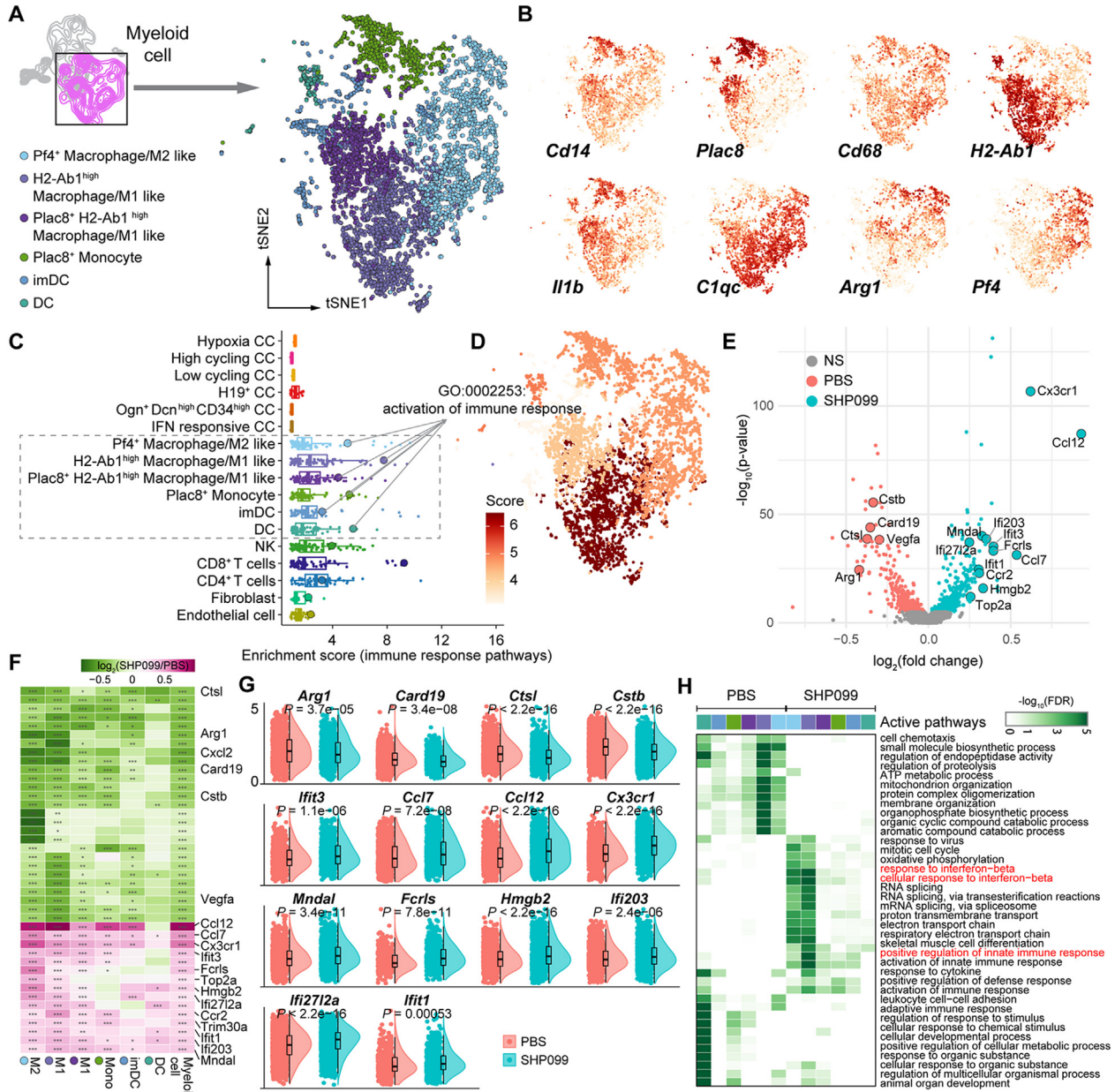


**Figure 5** Transcriptional diversity in myeloid cells. (A) t-SNE representation of myeloid cell sub-clusters. (B) t-SNE plots of selected marker expression. (C) Enrichment of “immune response” related pathways in different cell clusters (myeloid cell sub-clusters in the dashed box). Each dot denotes a specific gene ontology (GO) biological pathway. The pathway of “activation of immune response” (GO: 0002253) is highlighted in large dots, and the corresponding enrichment score for this pathway is visualized in the t-SNE plot in (D). (E) Volcano plot showing all genes that were differentially expressed (with corrected  $P$ -value  $< 1.0 \times 10^{-5}$ ) between PBS and SHP099. Example differentially expressed genes (DEGs) are highlighted. NS: not significant. (F) Heatmap showing top DEGs between PBS and SHP099. The average fold-change (FC) of each gene (row) in SHP099 relative to PBS cells was plotted for each sub-clusters (column). Pink indicates higher expression in SHP099 cells and green indicates higher expression in PBS cells. Raincloud plots (G) show expression difference for myeloid cells from PBS and SHP099 groups. (H) Gene set enrichment analysis (GSEA) applied on myeloid cell expression data by comparing cells from PBS and SHP099 groups. Heatmap shows the enrichment of top active GO pathways in PBS or SHP099 myeloid cells.

cells (Fig. 5E and G). Of note, the expression of genes (*Ccl7*, *Ifi11*, *Ifi3*, *Cx3cr1*, *Ifi203*, *Ifi2712a* and *Mndal*) associated with ‘classically activated’ (M1)<sup>45</sup> and type I interferon signaling response elevated, while *Arg1*, *Vegfa* and *Ctsl* belongs to ‘alternative activated’ (M2)<sup>45</sup> in TAMs abated. Thus, ‘response to interferon-beta’ pathway significantly activated after SHP099 treatment (Fig. 5H).

3.5. SHP2 negatively regulates type I interferon signaling

In APCs, the sensing of extracellular DNA is first dependent on phagocytosis<sup>46</sup>. However, both of two adverse phagocytosis checkpoints *Lrp1* and *Sirpa* expression were decreased, indicating that the immunosuppression role of SHP2 was not dependent on

influencing phagocytosis directly (Supporting Information Fig. S7). To confirm whether SHP2 act on type I interferon signaling directly, we performed experiments using allosteric inhibitor

SHP099 in THP-1-derived macrophage and BMDMs from *Ptpn11* *lyz2* knockout (KO) mice. (Fig. 6 and Supporting Information Fig. S8). THP-1-derived macrophages were simulated by 2',3'-cGAMP

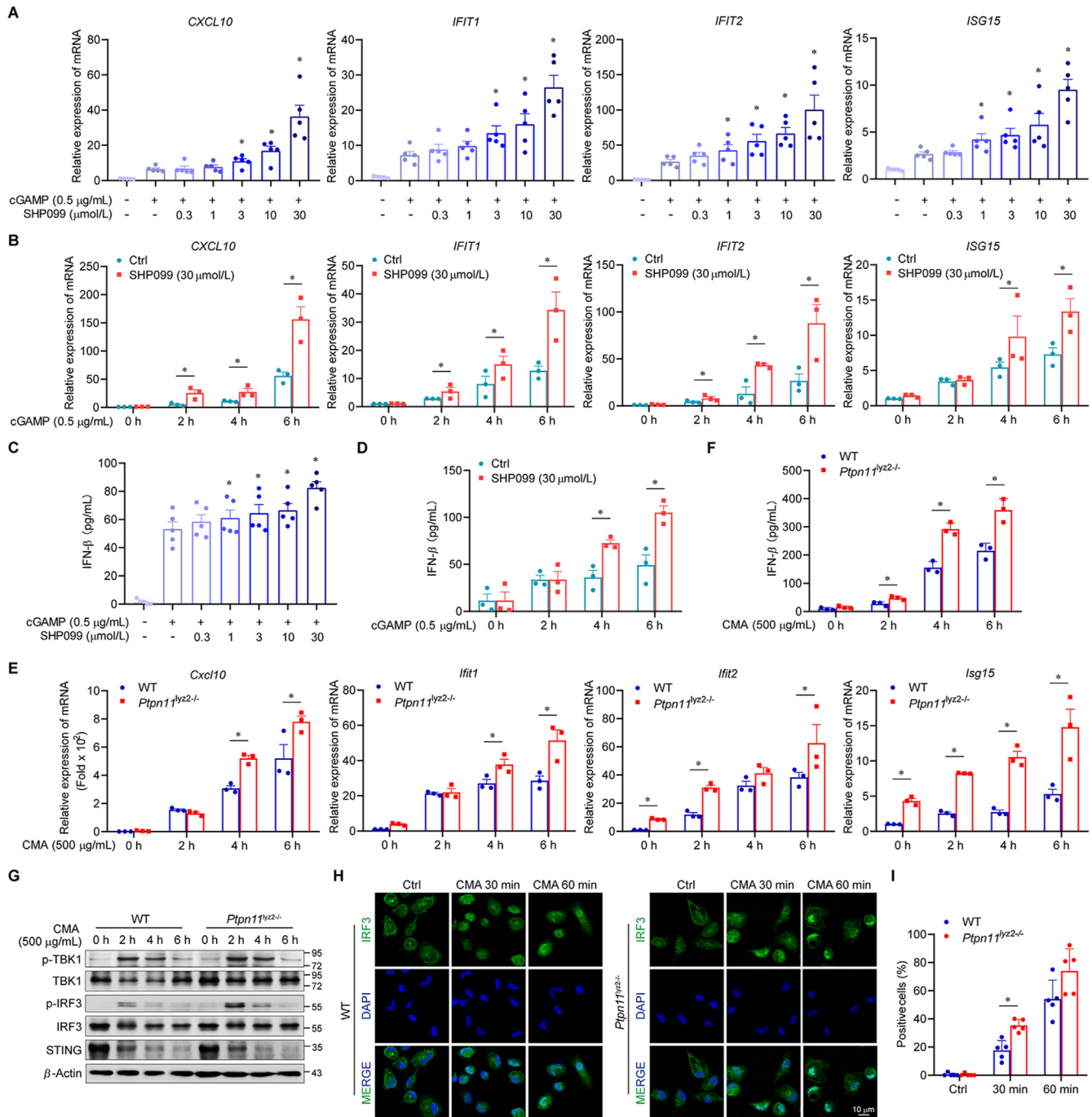


**Figure 6** SHP2 negatively regulates type I interferon signaling via STING–TBK1–IRF3 pathway. PMA-differentiated THP1 cells were simulated by 2',3'-cGAMP (0.5 μg/mL) for 2, 4, and 6 h or simulated by 2',3'-cGAMP for 4 h after incubation with or without the indicated concentrations of SHP099 for 1 h. (A, B) Relative mRNA expression of *CXCL10*, *IFIT1*, *IFIT2* and *ISG15* was examined by qPCR. (C, D) IFN-β in the supernatant were detected by ELISA. Primarily cultured BMDMs from WT and *Ptpn11<sup>lyz2-/-</sup>* were simulated by CMA (500 μg/mL) for 2, 4, or 6 h as indicated. (E) Relative mRNA expression of *Cxcl10*, *Ifit1*, *Ifit2* and *Isig15* were examined by qPCR. (F) IFN-β in the supernatant were detected by ELISA. Data represent mean ± SEM; (A) and (C): n = 5; (B, D–F): n = 3; \*P < 0.05. (G) Protein levels of p-TBK1, TBK1, p-IRF3, IRF3, STING and SHP2 were analyzed by Western blot. β-Actin was shown as loading control. (H) Primarily cultured BMDMs from WT and *Ptpn11<sup>lyz2-/-</sup>* were simulated by CMA (500 μg/mL) for 30 and 60 min as indicated. The subcellular localization of IRF3 (shown in green) was analyzed via confocal microscopy. Cell nuclei were visualized by DAPI (blue). Scale bar, 10 μm. (I) Percentage of the cells with IRF3 nuclear localization from Panel H. Data are shown as the mean ± SEM of five fields of view, \*P < 0.05.

for 4 h after incubation with or without the indicated concentrations of SHP099 or pre-treated with 30  $\mu\text{mol/L}$  SHP099 for 1 h before challenge with 2',3'-cGAMP (0.5  $\mu\text{g/mL}$ ) for 2, 4, and 6 h. The mRNA levels of several type I interferon inducible genes including *CXCL10*, *IFIT1*, *IFIT2*, *ISG15* (Fig. 6A and B) and also IFN- $\beta$  in the supernatants (Fig. 6C and D) were markedly elevated by SHP099 in both time- and dose-dependent manner.

To address the underlying mechanism, BMDMs from WT and *Pttn11<sup>lyz2-/-</sup>* mice were incubated with mouse-specific STING agonist 10-carboxymethyl-9-acridanone (CMA), as the results shown, the mRNA levels of *CXCL10*, *IFIT1*, *IFIT2*, *ISG15* and IFN- $\beta$  in the supernatants (Fig. 6E and F) were increased significantly upon SHP2 deletion. Moreover, SHP2 deletion attenuated CMA-induced phosphorylation of TBK1 and IRF3 (Fig. 6G) and IRF3 nuclear translocation (Fig. 6H). To confirm the role of SHP2 in TAMs *in vivo*, WT and *Pttn11<sup>lyz2-/-</sup>* mice were performed with murine MC38 colon cancer xenograft model. The tumor sizes and

weights in MC38 tumor-bearing *Pttn11<sup>lyz2-/-</sup>* mice displayed a conspicuous decrease (Fig. S8C and S8D). The anti-tumor immunity, including immune cell infiltration, has been displayed gradually weakening as the tumor size increases and SHP2 activation especially in macrophages. A maximum on Day 9 was observed and followed by a gradual decline in the percentages of CD8<sup>+</sup> T cell and CD86<sup>+</sup> macrophage. It suggested that Day 14 were more suitable for the distribution test of immune cells upon SHP099 treatment (Supporting Information Fig. S9). Then, we examined the immune microenvironment on Day 14. More immune cell infiltrations (including NK cells, T cells, and macrophages) and higher percentages of antitumor immune cell differentiation (CD8 T cells and M1 macrophages) were detected in SHP099 treated group and SHP2 conditional knockout group (Fig. 7A–D). Notably, the expressions of IFN- $\beta$  and *Ifnb1* in tumor tissue were enhanced obviously with the decreased levels of pSHP2 in CD86<sup>+</sup>F4/80<sup>+</sup> cells (Fig. 7E–G, and Fig. S8E–S8F).

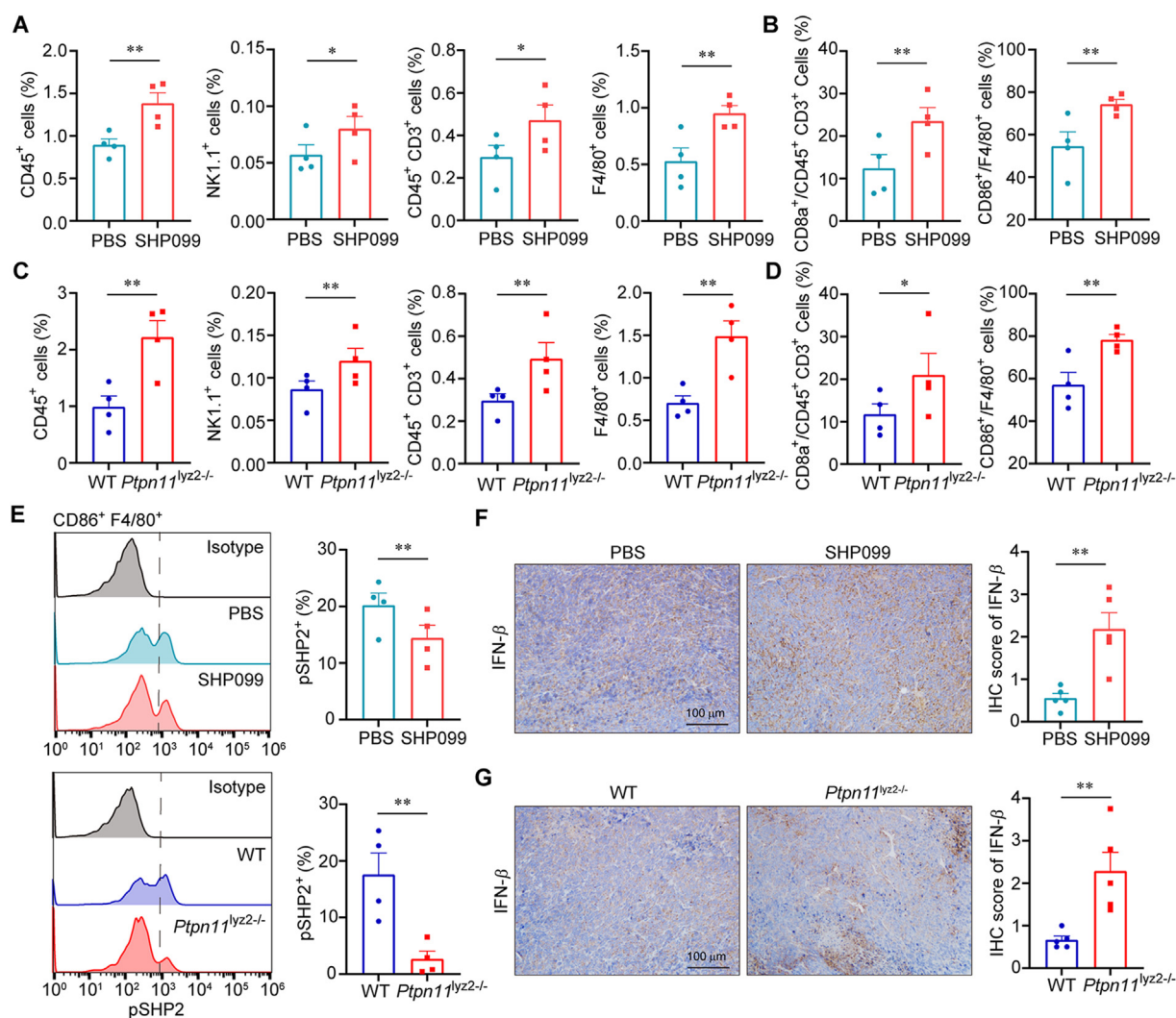


**Figure 7** Macrophagic SHP2 antagonizes IFN- $\beta$  expression and immune infiltration in TMEs. Flow cytometric quantification of the percentage of immune cells (CD45<sup>+</sup>), NK cells (NK1.1<sup>+</sup>), T cells (CD45<sup>+</sup>CD3<sup>+</sup>), and macrophages (F4/80<sup>+</sup>) in PBS and SHP099 groups (A) or WT and *Pttn11<sup>lyz2-/-</sup>* groups (C). CD8<sup>+</sup> T cells among CD45<sup>+</sup>CD3<sup>+</sup> cells and CD86<sup>+</sup> macrophages among F4/80<sup>+</sup> cells in the tumor tissues from PBS and SHP099 groups (B) or WT and *Pttn11<sup>lyz2-/-</sup>* groups (D). (E) Phosphorylation levels of SHP2 in CD86<sup>+</sup>F4/80<sup>+</sup> cells were measured and quantified by flow cytometry. Data represent mean  $\pm$  SEM,  $n = 4$ ; \* $P < 0.05$ , \*\* $P < 0.01$ . (F, G) Left, representative images of IFN- $\beta$  expression. Scale bar: 100  $\mu\text{m}$ . Right, IHC score. Data are shown as the mean  $\pm$  SEM,  $n = 5$ ; \*\* $P < 0.01$ .

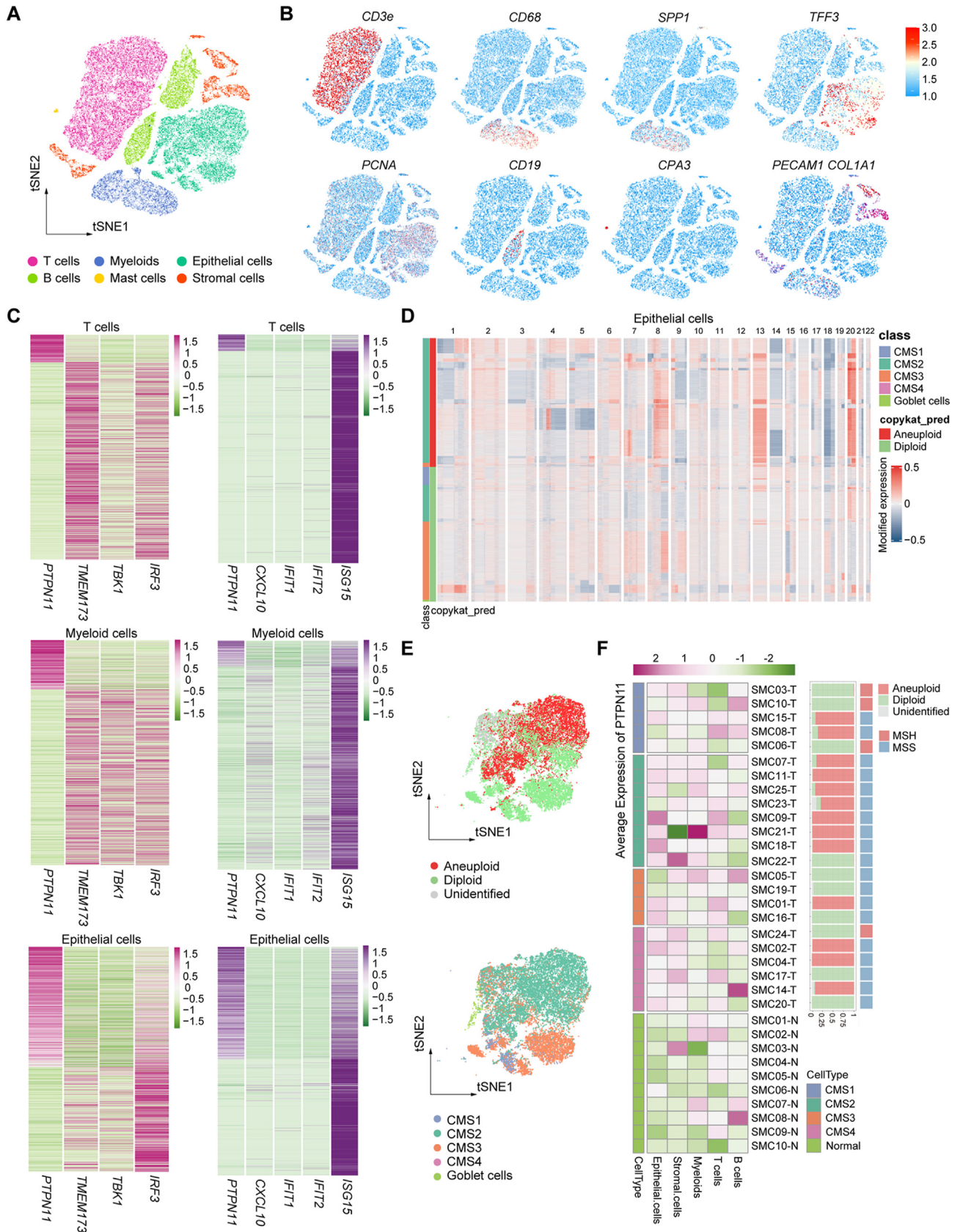


**Figure 8** The association of *PTPN11* and type I interferon signaling is verified using human colorectal cancer samples. Single cell RNA-seq dataset was obtained from GEO database (GSE132465) which contains 63,689 cells from 23 CRC patients (MSS, 19 patients; MSI-H, 4 patients) with 23 primary colorectal cancer and 10 matched normal mucosa samples. (A) t-SNE plot of all cells colored by their cell type (bottom). (B)

Taken together, SHP2 negatively regulates type I interferon signaling and antitumor immunity in mice.

### 3.6. The clinical relevance of macrophage-expressed phosphorylated SHP2

To further confirm the above results, a single cell RNA-seq dataset was downloaded from Gene Expression Omnibus (GEO) database which contains 63,689 cells from 23 CRC patients (MSS, 19 patients; MSI-H, 4 patients) with 23 primary colorectal cancer and 10 matched normal mucosa samples<sup>40</sup>. According to the details published, the cells were annotated as six major cell types including T cells, myeloid cells, epithelial cells, B cells, mast cells, and stromal cells, which are featured by marker gene *CD3e*, *CD68*, *SPPI1*, *TFF3*, *PNCA*, *CD19*, *CPA3*, *PECAMI1*, and *COL1A1* respectively (Fig. 8A and B). Notably, the *PTPN11* expressions in T cells, myeloid cells, and epithelial cells were negatively correlated with the expressions of type I interferon-inducible genes, even including upstream genes *TMEM173*, *TBK1*, and *IRF3* (Fig. 8C). After consensus molecular subtypes (CMS) and somatic copy number aberrations combined analysis, malignant cells were mainly concentrated in MSS subtypes, especially in CMS2 subtypes (Fig. 8D and E). CMS2 subtype (37% of all CRC) is commonly named ‘immune desert’ which is featured as poor intratumoral immune response with low levels of immune infiltration<sup>3</sup>. Importantly, *PTPN11* is highly expressed in T cells, myeloid cells, and epithelial cells rather than stromal cells and B cells in this subtype. In contrast, *PTPN11* expression, especially in myeloid cells, was relatively lower in the less malignant phenotypes including MSI-H subtype (Fig. 8F). These results indicate that there is a negative correlation between *PTPN11* and type I interferon signaling in myeloid cells from human colorectal cancer samples.

Therefore, the role of SHP2 in tumor-associated macrophage was indicated in colorectal cancer samples. We used TIMER algorithm to perform the cumulative survival of low/high immune infiltration level including lymphoid B cell, CD8<sup>+</sup> T cell and CD4<sup>+</sup> T cell or myeloid dendritic cell, macrophage and neutrophil in CRC patients. Compared to the other types of immune infiltration (Supporting Information Fig. S10A and S10B), macrophage infiltration level displayed a significant negative correlation with cumulative survival (Fig. 9A). Moreover, *Ptpn11* expression showed a significant positive correlation with the levels of several pro-tumor genes *MRC1*, *CTST* and *MMP9* in TAMs (Fig. 9B). However, total *Ptpn11* expression displayed a negative correlation with cumulative survival (Fig. S10C), indicated a potential role of SHP2 in other cell types that still need to be further explored. Next, we collected colon cancer tissue samples from 35 CRC patients, including 23 MSS phenotypes and 12 MSI-H phenotypes. These two groups were similar for gender composition and average age (Supporting Information Fig. S11). Immunofluorescence was performed for detecting infiltration of macrophages and the phosphorylation level of SHP2 (Fig. 9C). The percentage of

infiltrated macrophages was positively correlated with the age of the patients (Fig. 9D). Moreover, MSS phenotypes of CRC patients displayed more infiltrated CD68<sup>+</sup> macrophages and more potent phosphorylation of SHP2 in macrophages than MSI-H phenotypes (Fig. 9E and H). These findings indicate that more attention should be paid to SHP2-mediated innate immunosuppression for older CRC patients. Notably, IFN- $\beta$  expression was lower in MSS phenotypes (Fig. 9F and I) and negatively correlated with the phosphorylation of SHP2 in macrophages (Fig. 9G). To sum up, our results reveal that TME remodeling by inhibition of over-activated SHP2 in TAMs is a potential strategy for colon cancer therapy.

## 4. Discussion

Tyrosine phosphatase SHP2 has been extensively studied as an oncoprotein in the downstream of RAS/MAPK pathway. Moreover, a broad spectrum of mutation of this protein was found in human diseases<sup>15,19</sup>. So the inhibitors against catalytic sites in SHP2 has developed for many years. But in general, increased tyrosine phosphorylation activity is a hallmark of many cancers, and PTPs are considered as negative regulators of signaling pathways and tumor suppressor genes, such as tumor suppressor PTEN (phosphatase and tensin homolog). Therefore, none of PTP inhibitors has advanced to clinical due to the unacceptable potency/selectivity<sup>29</sup>. Nowadays, allosteric inhibition has become a novel strategy to selectively target SHP2 for tumor treatment. Specially, allosteric inhibitors including SHP099 can lock the PTP and N-SH2 domain interaction to maintain the auto-inhibited conformation for SHP2 blockade selectively<sup>24</sup>. What's more, Zhu et al.<sup>47</sup> uncovered a common well-folded PTP domain dependent liquid–liquid phase separation (LLPS) behavior in both enzymatically activating and inactivating disease-associated SHP2 mutants. The LLPS was regulated by multivalent electrostatic interactions and intrinsic conformational changes which reflects the huge application advantages of allosteric inhibitors.

Considering the diverse known role of SHP2<sup>23,48–50</sup>, we tried to explore the global role of SHP2 in TMEs by performing single-cell RNA sequencing with allosteric inhibitor SHP099 treatment. At first, we observed SHP099 restrict cancer malignant evolution by pseudotime analysis and some interesting genes dynamics (Fig. 3). Among the differentially expressed genes, the expressions of JUN/FOS heterodimer complex (*Jund*, *June*, *Fos*, *Fosb*), especially *Fos*, were higher in SHP099 group (Fig. 2B and C). c-FOS (encoded by *FOS*) is known as a downstream gene product of ERK to form activator protein 1 (AP-1) transcription factor participating in cell proliferation, transformation, death, immune response and chemoresistant<sup>51–54</sup>. Usually, the inhibition of SHP2 can lead to ERK inhibition and *FOS* down-regulation. Interestingly, O’Flanagan et al.<sup>55</sup> reported hundreds heat shock and stress response genes, including *FOS* and *JUN* induced when tissue dissociated by collagenase at 37 °C. While in our data, we did not find this phenomenon in other cell types. Therefore, we speculated

Expression of example marker genes. (C) Heatmap of the expression level of *PTPN11* and type I interferon inducible genes of T cells, myeloid cells and epithelial cells. (D) Landscape of inferred large-scale chromosomal copy number variations (CNVs) distinguishing diploid cells and aneuploidy cells. Gained (red) or loss (blue) CNVs were inferred in each chromosome. Cancer cell sub-clusters are colored according to cell types. Cluster analysis divided the cells into two parts and the cells in red bar with extensive genome-wide copy number aberrations were considered as malignant cells. (E) t-SNE plot of all selected cells colored by predicted results in (D) and their cell type. Unidentified cells mean the invalid cells was filtered. (F) Left, average expression of *PTPN11* of all samples in all major cell types. Right, Barplot showing the proportion of diploids, aneuploidy and unidentified cells in each tumor tissue with the MSH or MSS type annotating.

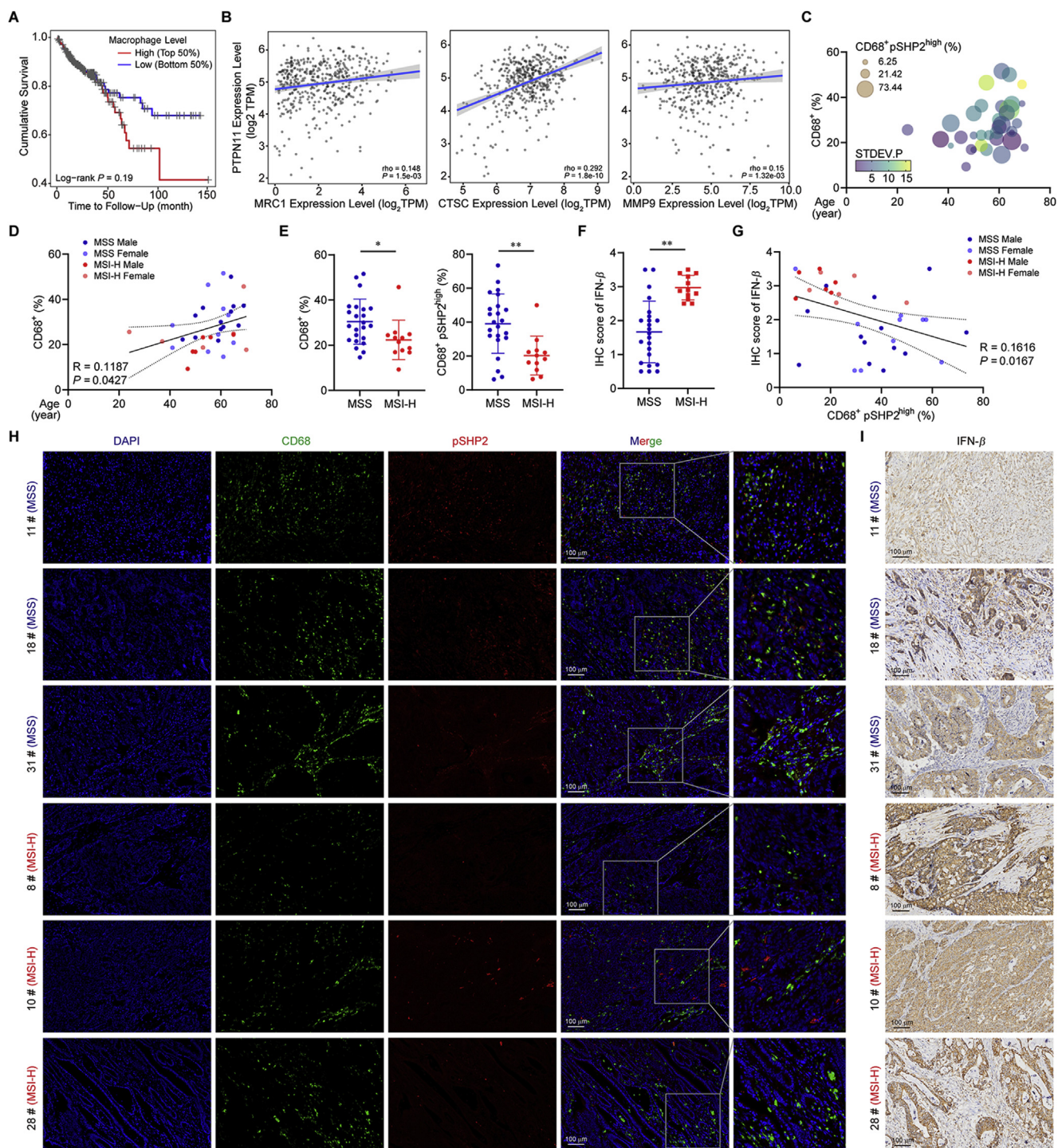


**Figure 9** Oncogenic role of SHP2 in tumor-associated macrophage of colon cancer. (A) Cumulative survival of low and high macrophage infiltration level in CRC patients *via* TIMER algorithm. (B) The correlations between *PTPN11* and *MRC1*, *CTSC*, *MMP9* were performed by Gene\_Corr module on TIMER website. The expression of CD68 (shown in green) and p-SHP2 (Y542, shown in red) of section samples from CRC patients were analyzed *via* confocal microscopy. Cell nuclei were visualized by DAPI (blue). Total cell numbers, the numbers of CD68<sup>+</sup> and CD68<sup>+</sup> pSHP2<sup>high</sup> population were analyzed by ImageJ followed by visualized with bubble map (C). (D) Linear regression correlation analysis of CD68<sup>+</sup> cell infiltration level and patients' age. MSS group was shown in blue and MSI-high group was shown in red. (E) The percentage of CD68<sup>+</sup> and CD68<sup>+</sup> pSHP2<sup>high</sup> population in the tissue samples. (F) IHC scores of IFN- $\beta$ . (G) Linear regression correlation analysis of IFN- $\beta$  IHC scores and CD68<sup>+</sup> pSHP2<sup>high</sup> population. Data represent mean  $\pm$  SEM, MSS:  $n = 23$ , MSI-H:  $n = 12$ ; \* $P < 0.05$ , \*\* $P < 0.01$ . Representative IF (H) and IHC (I) images of MSS and MSI-H groups. Scale bar, 100  $\mu$ m.

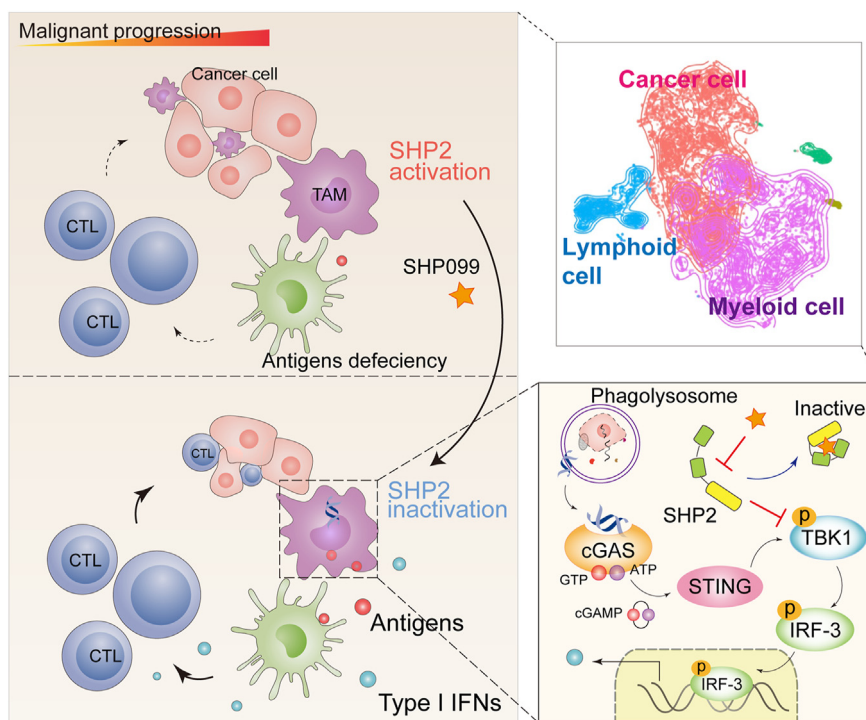


**Figure 10** The graphic illustration of the mechanism of SHP2-mediated tumor immunosuppression in colon cancer defined by single-cell RNA sequencing. All cell types of tumor microenvironment (TME) from murine MC38 xenograft tumors upon SHP099 treatment were investigated by single-cell transcriptomics. SHP2 negatively regulates type I interferon signaling by preventing STING–TBK1–IRF3 signaling pathway in tumor-associated macrophages. SHP2 allosteric inhibition remodels the anti-tumor TME, indicating that SHP2 is a promising target for colon cancer immunotherapy.

it maybe an intrinsic develop response of tumor to SHP099 treatment or increased IFN- $\beta$  expression in TMEs or stronger CD8<sup>+</sup> T cell-induced cytotoxicity, which is required to be further investigated.

The previous work of our group revealed SHP2 deletion and inhibition in T cells triggered an anti-tumor immunity<sup>30,31</sup>. In this study, we reveal that SHP099 treatment enhanced type I interferon signaling in CD8<sup>+</sup> T cell and triggered NK cell activation (Fig. 4). Notably, Li et al.<sup>56</sup> reported intrinsic cGAS–STING-mediated type I interferon signaling in T cell can promote the maintenance of stem cell-like CD8<sup>+</sup> T cell. NK cells were also reported to be activated in an type I interferon induced IL-15-dependent manner which provides another option to target the tumors with low neoantigens or class I MHC expression deficiency evade CD8<sup>+</sup> T cell cells<sup>57</sup>. All of them provides insight into the development of improved lymphocytes cell therapy targeting SHP2 involved type I interferon signaling. Meanwhile, we noticed Elsa Quintana et al.<sup>58</sup> reported additional functions for SHP2 beyond checkpoint transduction in T cells when observed the combination of SHP2 inhibition and checkpoint immunotherapy. They found that SHP2 inhibition produced a direct depletion of protumorigenic M2 macrophages by CSF1 receptor (CSF1R) signaling blockade. Here, we demonstrate SHP099 enhanced type I interferon signaling in macrophages by regulating STING–TBK1–IRF3 pathway (Figs. 5 and 6). Significantly, a study before investigated SHP2-mediated E3 ubiquitin ligase TRIM27-induced TBK1 degradation, a similar mechanism in host antiviral innate immune responses<sup>59</sup>. Moreover, SHP-2 was reported to bind to the kinase domain of TBK1 directly by C-terminal domain (273–538,

including PTP domain) SHP-2 and inhibit phosphorylation of substrate by TBK1<sup>60</sup>, which supported our results. TBK1 was found to be more dephosphorylated and degraded in WT group than *Ptpn11*<sup>lyz-/-</sup> group after stimulation for 2 and 4 h (Fig. 6G). However, they thought SHP-2 inhibited the activity of TBK1 through a tyrosine phosphatase activity-independent mechanism, because mutation of C463S, which disrupted the tyrosine phosphatase activity of SHP-2, did not reverse the inhibition of poly (I:C)-induced IFN- $\beta$  production and TBK1-activated IFN- $\beta$  reporter gene expression. But we think more evidence is needed for this conclusion, especially the discovery of mutant SHP2-mediated WT SHP2 activation by LLPS<sup>47</sup>. Additionally, a recent study reported a totally opposite role of SHP2 in TAMs of CRC. They found absence of SHP2 on TAMs result in M2 phenotype polarization. But the cell line they used CT26 is BALB/c mice colon adenocarcinoma cell line, which is not appropriate for the experiments with C57BL/6 mice<sup>61</sup>.

Compared to MSI-H phenotype, MSS in colon cancer features as neoantigens deficiency, immune resistance and implies unfavorable response to immune checkpoint blockade therapy<sup>3</sup>. However, the molecular nature of phenotypes is not well elucidated. Recently, Bao et al. investigated the molecular features in MSI and MSS colon cancer at the single-cell level. They found higher abundance of exhausted CD8<sup>+</sup> T cells, activated NK cells, and M1 macrophages in MSI colon cancer rather than MSS colon cancer<sup>62</sup>. However, they analyzed the lymphocytes and malignant cells features without myeloid cells which took up a large percentage of global clusters, especially in MSS group. In contrast, our results suggest that SHP2 phosphorylation in APCs acts as a

cause of innate immunosuppression that leads to neoantigens deficiency and limited immune cells infiltration (Figs. 8, 9C and 9H).

## 5. Conclusions

Our study reveals SHP2-mediated innate immunosuppression in colon cancer microenvironment. SHP2 allosteric inhibition remodels the anti-tumor TME which indicated that SHP2 is a promising target for colon cancer immunotherapy (Fig. 10).

## Acknowledgments

We thank Prof. Gen-Sheng Feng (University of California San Diego, CA, USA) for presenting *Ptpn11<sup>fllox/fllox</sup>* mice. This work was supported by National Natural Science Foundation of China (Nos. 91853109, 81730100, 81872877, and 81673436), and Mountain-Climbing Talents Project of Nanjing University (China).

## Author contributions

Yang Sun and Qiang Xu conceived and supervised the study. Jian Gao, Mingxia Zhao, and Manru Li performed the cell line experiments and animal experiments and analyzed the data. Zhigui Wu, Xianjia Qi, and Dijun Chen performed bioinformatics analysis. Hongqi Chen and Rui Zhang provided clinical samples. Dongdong Sun, Haibo Cheng and Yuxian Shen gave methodological support and conceptual advice. Jian Gao and Yang Sun wrote the manuscript. All authors discussed the results and commented on the manuscript.

## Conflicts of interest

The authors declare no conflicts of interest.

## Appendix A. Supporting information

Supporting data to this article can be found online at <https://doi.org/10.1016/j.apsb.2021.08.006>.

## References

- Bray F, Ferlay J, Soerjomataram I, Siegel RL, Torre LA, Jemal A. Global cancer statistics 2018: GLOBOCAN estimates of incidence and mortality worldwide for 36 cancers in 185 countries. *CA Cancer J Clin* 2018;**68**:394–424.
- Bonnot PE, Passot G. RAS mutation: site of disease and recurrence pattern in colorectal cancer. *Chin Clin Oncol* 2019;**8**:55.
- Picard E, Verschoor CP, Ma GW, Pawelec G. Relationships between immune landscapes, genetic subtypes and responses to immunotherapy in colorectal cancer. *Front Immunol* 2020;**11**:369.
- Gurjao C, Liu D, Hofree M, AlDubayan SH, Wakiro I, Su MJ, et al. Intrinsic resistance to immune checkpoint blockade in a mismatch repair-deficient colorectal cancer. *Cancer Immunol Res* 2019;**7**:1230–6.
- Ablasser A, Hur S. Regulation of cGAS- and RLR-mediated immunity to nucleic acids. *Nat Immunol* 2020;**21**:17–29.
- Woo SR, Fuertes MB, Corrales L, Spranger S, Furdyna MJ, Leung MY, et al. STING-dependent cytosolic DNA sensing mediates innate immune recognition of immunogenic tumors. *Immunity* 2014;**41**:830–42.
- Marcus A, Mao AJ, Lensink-Vasan M, Wang L, Vance RE, Raulet DH. Tumor-derived cGAMP triggers a STING-mediated interferon response in non-tumor cells to activate the nk cell response. *Immunity* 2018;**49**:754–763.e4.
- Chon HJ, Kim H, Noh JH, Yang H, Lee WS, Kong SJ, et al. STING signaling is a potential immunotherapeutic target in colorectal cancer. *J Cancer* 2019;**10**:4932–8.
- Su T, Zhang Y, Valerie K, Wang XY, Lin S, Zhu G. STING activation in cancer immunotherapy. *Theranostics* 2019;**9**:7759–71.
- Reislander T, Groelly FJ, Tarsounas M. DNA damage and cancer immunotherapy: a STING in the tale. *Mol Cell* 2020;**80**:21–8.
- Feng GS, Hui CC, Pawson T. SH2-containing phosphotyrosine phosphatase as a target of protein-tyrosine kinases. *Science* 1993;**259**:1607–11.
- Dechert U, Duncan AM, Bastien L, Duff C, Adam M, Jirik FR. Protein-tyrosine phosphatase SH-PTP2 (PTPN11) is localized to 12q24.1-24.3. *Hum Genet* 1995;**96**:609–15.
- Barford D, Neel BG. Revealing mechanisms for SH2 domain mediated regulation of the protein tyrosine phosphatase SHP-2. *Structure* 1998;**6**:249–54.
- Hof P, Pluskey S, Dhe-Paganon S, Eck MJ, Shoelson SE. Crystal structure of the tyrosine phosphatase SHP-2. *Cell* 1998;**92**:441–50.
- Tartaglia M, Niemeyer CM, Fragale A, Song X, Buechner J, Jung A, et al. Somatic mutations in PTPN11 in juvenile myelomonocytic leukemia, myelodysplastic syndromes and acute myeloid leukemia. *Nat Genet* 2003;**34**:148–50.
- Aceto N, Sausgruber N, Brinkhaus H, Gaidatzis D, Martiny-Baron G, Mazzarol G, et al. Tyrosine phosphatase SHP2 promotes breast cancer progression and maintains tumor-initiating cells via activation of key transcription factors and a positive feedback signaling loop. *Nat Med* 2012;**18**:529–37.
- Choi E, Kikuchi S, Gao H, Brodzik K, Nassour I, Yopp A, et al. Mitotic regulators and the SHP2–MAPK pathway promote IR endocytosis and feedback regulation of insulin signaling. *Nat Commun* 2019;**10**:1473.
- Liu W, Yin Y, Wang M, Fan T, Zhu Y, Shen L, et al. Disrupting phosphatase SHP2 in macrophages protects mice from high-fat diet-induced hepatic steatosis and insulin resistance by elevating IL-18 levels. *J Biol Chem* 2020;**295**:10842–56.
- Tartaglia M, Mehler EL, Goldberg R, Zampino G, Brunner HG, Kremer H, et al. Mutations in PTPN11, encoding the protein tyrosine phosphatase SHP-2, cause Noonan syndrome. *Nat Genet* 2001;**29**:465–8.
- Matozaki T, Murata Y, Saito Y, Okazawa H, Ohnishi H. Protein tyrosine phosphatase SHP-2: a proto-oncogene product that promotes Ras activation. *Cancer Sci* 2009;**100**:1786–93.
- Gavrieli M, Watanabe N, Loftin SK, Murphy TL, Murphy KM. Characterization of phosphotyrosine binding motifs in the cytoplasmic domain of B and T lymphocyte attenuator required for association with protein tyrosine phosphatases SHP-1 and SHP-2. *Biochem Biophys Res Commun* 2003;**312**:1236–43.
- Yokosuka T, Takamatsu M, Kobayashi-Imanishi W, Hashimoto-Tane A, Azuma M, Saito T. Programmed cell death 1 forms negative costimulatory microclusters that directly inhibit T cell receptor signaling by recruiting phosphatase SHP2. *J Exp Med* 2012;**209**:1201–17.
- Liu Q, Qu J, Zhao M, Xu Q, Sun Y. Targeting SHP2 as a promising strategy for cancer immunotherapy. *Pharmacol Res* 2020;**152**:104595.
- Chen YN, LaMarche MJ, Chan HM, Fekkes P, Garcia-Fortanet J, Acker MG, et al. Allosteric inhibition of SHP2 phosphatase inhibits cancers driven by receptor tyrosine kinases. *Nature* 2016;**535**:148–52.
- Dardaei L, Wang HQ, Singh M, Fordjour P, Shaw KX, Yoda S, et al. SHP2 inhibition restores sensitivity in ALK-rearranged non-small-cell lung cancer resistant to ALK inhibitors. *Nat Med* 2018;**24**:512–7.
- LaRochelle JR, Fodor M, Vemulapalli V, Mohseni M, Wang P, Stams T, et al. Structural reorganization of SHP2 by oncogenic mutations and implications for oncoprotein resistance to allosteric inhibition. *Nat Commun* 2018;**9**:4508.
- Padua RAP, Sun Y, Marko I, Pitsawong W, Stiller JB, Otten R, et al. Mechanism of activating mutations and allosteric drug inhibition of the phosphatase SHP2. *Nat Commun* 2018;**9**:4507.

28. Wong GS, Zhou J, Liu JB, Wu Z, Xu X, Li T, et al. Targeting wild-type KRAS-amplified gastroesophageal cancer through combined MEK and SHP2 inhibition. *Nat Med* 2018;**24**:968–77.
29. Yuan X, Bu H, Zhou J, Yang CY, Zhang H. Recent advances of SHP2 inhibitors in cancer therapy: current development and clinical application. *J Med Chem* 2020;**63**:11368–96.
30. Liu W, Guo W, Shen L, Chen Z, Luo Q, Luo X, et al. T lymphocyte SHP2-deficiency triggers anti-tumor immunity to inhibit colitis-associated cancer in mice. *Oncotarget* 2017;**8**:7586–97.
31. Zhao M, Guo W, Wu Y, Yang C, Zhong L, Deng G, et al. SHP2 inhibition triggers anti-tumor immunity and synergizes with PD-1 blockade. *Acta Pharm Sin B* 2019;**9**:304–15.
32. Butler A, Hoffman P, Smibert P, Papalexi E, Satija R. Integrating single-cell transcriptomic data across different conditions, technologies, and species. *Nat Biotechnol* 2018;**36**:411–20.
33. Hafemeister C, Satija R. Normalization and variance stabilization of single-cell RNA-seq data using regularized negative binomial regression. *Genome Biol* 2019;**20**:296.
34. Stuart T, Butler A, Hoffman P, Hafemeister C, Papalexi E, Mauck 3rd WM, et al. Comprehensive integration of single-cell data. *Cell* 2019;**177**:1888–902.e21.
35. Durinck S, Moreau Y, Kasprzyk A, Davis S, De Moor B, Brazma A, et al. BioMart and Bioconductor: a powerful link between biological databases and microarray data analysis. *Bioinformatics* 2005;**21**:3439–40.
36. Durinck S, Spellman PT, Birney E, Huber W. Mapping identifiers for the integration of genomic datasets with the R/Bioconductor package biomaRt. *Nat Protoc* 2009;**4**:1184–91.
37. Qiu X, Hill A, Packer J, Lin D, Ma YA, Trapnell C. Single-cell mRNA quantification and differential analysis with Census. *Nat Methods* 2017;**14**:309–15.
38. Qiu X, Mao Q, Tang Y, Wang L, Chawla R, Pliner HA, et al. Reversed graph embedding resolves complex single-cell trajectories. *Nat Methods* 2017;**14**:979–82.
39. Gao J, Fan M, Xiang G, Wang J, Zhang X, Guo W, et al. Diptoindonesin G promotes ERK-mediated nuclear translocation of p-STAT1 (Ser727) and cell differentiation in AML cells. *Cell Death Dis* 2017;**8**:e2765.
40. Lee HO, Hong Y, Etioglu HE, Cho YB, Pomella V, Van den Bosch B, et al. Lineage-dependent gene expression programs influence the immune landscape of colorectal cancer. *Nat Genet* 2020;**52**:594–603.
41. Gao R, Bai S, Henderson YC, Lin Y, Schalck A, Yan Y, et al. Delineating copy number and clonal substructure in human tumors from single-cell transcriptomes. *Nat Biotechnol* 2021;**39**:599–608.
42. Whitfield ML, George LK, Grant GD, Perou CM. Common markers of proliferation. *Nat Rev Cancer* 2006;**6**:99–106.
43. Zhang L, Li Z, Skrzypczynska KM, Fang Q, Zhang W, O'Brien SA, et al. Single-cell analyses inform mechanisms of myeloid-targeted therapies in colon cancer. *Cell* 2020;**181**:442–59.e29.
44. Elyada E, Bolisetty M, Laise P, Flynn WF, Courtois ET, Burkhart RA, et al. Cross-species single-cell analysis of pancreatic ductal adenocarcinoma reveals antigen-presenting cancer-associated fibroblasts. *Cancer Discov* 2019;**9**:1102–23.
45. Azizi E, Carr AJ, Plitas G, Cornish AE, Konopacki C, Prabhakaran S, et al. Single-cell map of diverse immune phenotypes in the breast tumor microenvironment. *Cell* 2018;**174**:1293–308.e36.
46. Feng M, Jiang W, Kim BYS, Zhang CC, Fu YX, Weissman IL. Phagocytosis checkpoints as new targets for cancer immunotherapy. *Nat Rev Cancer* 2019;**19**:568–86.
47. Zhu G, Xie J, Kong W, Xie J, Li Y, Du L, et al. Phase separation of disease-associated SHP2 mutants underlies MAPK hyperactivation. *Cell* 2020;**183**:490–502.e18.
48. Guo W, Liu W, Chen Z, Gu Y, Peng S, Shen L, et al. Tyrosine phosphatase SHP2 negatively regulates NLRP3 inflammasome activation via ANTI1-dependent mitochondrial homeostasis. *Nat Commun* 2017;**8**:2168.
49. Xiao P, Guo Y, Zhang H, Zhang X, Cheng H, Cao Q, et al. Myeloid-restricted ablation of Shp2 restrains melanoma growth by amplifying the reciprocal promotion of CXCL9 and IFN-gamma production in tumor microenvironment. *Oncogene* 2018;**37**:5088–100.
50. Xiao P, Zhang H, Zhang Y, Zheng M, Liu R, Zhao Y, et al. Phosphatase Shp2 exacerbates intestinal inflammation by disrupting macrophage responsiveness to interleukin-10. *J Exp Med* 2019;**216**:337–49.
51. Deng T, Karin M. c-Fos transcriptional activity stimulated by H-Ras-activated protein kinase distinct from JNK and ERK. *Nature* 1994;**371**:171–5.
52. Shaulian E, Karin M. AP-1 as a regulator of cell life and death. *Nat Cell Biol* 2002;**4**:E131–6.
53. Atsaves V, Leventaki V, Rassidakis GZ, Claret FX. AP-1 Transcription factors as regulators of immune responses in cancer. *Cancers* 2019;**11**:1037.
54. Bi M, Zhang Z, Jiang YZ, Xue P, Wang H, Lai Z, et al. Enhancer reprogramming driven by high-order assemblies of transcription factors promotes phenotypic plasticity and breast cancer endocrine resistance. *Nat Cell Biol* 2020;**22**:701–15.
55. O'Flanagan CH, Campbell KR, Zhang AW, Kabeer F, Lim JLP, Biele J, et al. Dissociation of solid tumor tissues with cold active protease for single-cell RNA-seq minimizes conserved collagenase-associated stress responses. *Genome Biol* 2019;**20**:210.
56. Li W, Lu L, Lu J, Wang X, Yang C, Jin J, et al. cGAS–STING-mediated DNA sensing maintains CD8<sup>+</sup> T cell stemness and promotes antitumor T cell therapy. *Sci Transl Med* 2020;**12**:eaay9013.
57. Nicolai CJ, Wolf N, Chang IC, Kirn G, Marcus A, Ndubaku CO, et al. NK cells mediate clearance of CD8<sup>+</sup> T cell-resistant tumors in response to STING agonists. *Sci Immunol* 2020;**5**:eaaz2738.
58. Quintana E, Schulze CJ, Myers DR, Choy TJ, Mordec K, Wildes D, et al. Allosteric inhibition of SHP2 stimulates antitumor immunity by transforming the immunosuppressive environment. *Cancer Res* 2020;**80**:2889–902.
59. Zheng Q, Hou J, Zhou Y, Yang Y, Xie B, Cao X. Siglec1 suppresses antiviral innate immune response by inducing TBK1 degradation via the ubiquitin ligase TRIM27. *Cell Res* 2015;**25**:1121–36.
60. An H, Zhao W, Hou J, Zhang Y, Xie Y, Zheng Y, et al. SHP-2 phosphatase negatively regulates the TRIF adaptor protein-dependent type I interferon and proinflammatory cytokine production. *Immunity* 2006;**25**:919–28.
61. Wang S, Yao Y, Li H, Zheng G, Lu S, Chen W. Tumor-associated macrophages (TAMs) depend on Shp2 for their anti-tumor roles in colorectal cancer. *Am J Cancer Res* 2019;**9**:1957–69.
62. Bao X, Zhang H, Wu W, Cheng S, Dai X, Zhu X, et al. Analysis of the molecular nature associated with microsatellite status in colon cancer identifies clinical implications for immunotherapy. *J Immunother Cancer* 2020;**8**:e001437.